TKK Dissertations 131
Espoo 2008

ORBIT-FOLLOWING SIMULATION OF FAST IONS IN ASDEX UPGRADE TOKAMAK IN THE PRESENCE OF MAGNETIC RIPPLE AND RADIAL ELECTRIC FIELD

Doctoral Dissertation

Ville Hynönen

Helsinki University of Technology
Faculty of Information and Natural Sciences
Department of Engineering Physics

TKK Dissertations 131
Espoo 2008

ORBIT-FOLLOWING SIMULATION OF FAST IONS IN ASDEX UPGRADE TOKAMAK IN THE PRESENCE OF MAGNETIC RIPPLE AND RADIAL ELECTRIC FIELD

Doctoral Dissertation

Ville Hynönen

Dissertation for the degree of Doctor of Science in Technology to be presented with due permission of the Faculty of Information and Natural Sciences for public examination and debate in Auditorium K216 at Helsinki University of Technology (Espoo, Finland) on the 18th of August, 2008, at 12 noon.

Helsinki University of Technology
Faculty of Information and Natural Sciences
Department of Engineering Physics

Teknillinen korkeakoulu
Informaatio- ja luonnontieteiden tiedekunta
Teknillisen fysiikan laitos

Distribution:
Helsinki University of Technology
Faculty of Information and Natural Sciences
Department of Engineering Physics
P.O. Box 4100
FI - 02015 TKK
FINLAND
URL: http://www.tkk.fi/Units/AES/
Tel. +358-9-451 3198
Fax +358-9-451 3195
E-mail: ville.hynonen@tkk.fi

ISBN 978-951-22-9458-9
ISBN 978-951-22-9459-6 (PDF)
ISSN 1795-2239
ISSN 1795-4584 (PDF)
URL: http://lib.tkk.fi/Diss/2008/isbn9789512294596/

TKK-DISS-2494

Multiprint Oy
Espoo 2008

ABSTRACT OF DOCTORAL DISSERTATION	HELSINKI UNIVERSITY OF TECHNOLOGY P. O. BOX 1000, FI-02015 TKK http://www.tkk.fi

Author Ville Hynönen

Name of the dissertation

Orbit-following simulation of fast ions in ASDEX Upgrade tokamak in the presence of magnetic ripple and radial electric field

Manuscript submitted April 1st, 2008	Manuscript revised
Date of the defence August 18th, 2008	
☐ Monograph	☑ Article dissertation (summary + original articles)
Faculty	Faculty of Information and Natural Sciences
Department	Department of Engineering Physics
Field of research	Fusion and Plasma Physics
Opponent(s)	Prof. Klaus Schöpf
Supervisor	Prof. Rainer Salomaa
Instructor	PhD Taina Kurki-Suonio

Abstract

Magnetic confinement of plasma inside a tokamak is presently the most promising form of controlled fusion. A key issue for future fusion devices such as ITER is the interaction between the hot plasma and the cold material surfaces. The density control and exhaust of impurities must be effected in a way not causing excessive heat and particle loads. Edge localized modes (ELMs), intermittent bursts of energy and particles, characterize the standard high confinement (H)-mode. In the recently discovered quiescent H-mode (QH-mode), they are replaced by so-called edge harmonic oscillations of a more continuous nature. The QH-mode is obtained only with counter-injected neutral beams, indicating that fast ions may affect the edge stability properties and thus ELMs.

In this thesis, the neutral-beam-originated fast ions in ASDEX Upgrade tokamak are modelled using the orbit-following Monte Carlo code ASCOT. The modelling results include the edge fast ion slowing-down distribution and the surface loads caused by fast ion losses for co- and counter-injected neutral beams, corresponding to H-mode and QH-mode, respectively. The effects of magnetic field ripple, arising from the finite number of toroidal field coils, and radial electric field E_r are included in the analysis. In addition to neutral beam ions, also the relation of surface distribution of tritium and the flux of tritons created in deuterium-deuterium fusion reactions is addressed.

Due to the difference in the direction of the gradient drift, counter-injected beams are prone to higher losses than co-injected beams. This leads to substantial wall loads, but also to higher edge fast ion density. Also the distribution of the fast ions in velocity space is different. The ripple-induced stochastic diffusion increases the losses, thereby increasing the wall load and reducing the density. The orbit width effects, squeezing for counter-injected and widening for co-injected beams, and orbit transitions caused by E_r further increase the losses and wall load. Nevertheless, they also lead to higher edge fast ion density and changes in the velocity distribution. The obtained 4D distribution functions could be used for gaining insight into the roots of the QH-mode by analyzing the stability properties of the edge for the two injection directions.

Keywords	fusion, tokamak, Monte Carlo methods, fast particle effects, ASCOT code		
ISBN (printed)	978-951-22-9458-9	ISSN (printed)	1795-2239
ISBN (pdf)	978-951-22-9459-6	ISSN (pdf)	1795-4584
Language	English	Number of pages	38 + app. 80
Publisher	Helsinki University of Technology		
Print distribution	Department of Engineering Physics, P.O. Box 4100, FI-02015 TKK, Finland		
☑ The dissertation can be read at http://lib.tkk.fi/Diss/2008/isbn9789512294596/			

VÄITÖSKIRJAN TIIVISTELMÄ	TEKNILLINEN KORKEAKOULU PL 1000, 02015 TKK http://www.tkk.fi

Tekijä Ville Hynönen

Väitöskirjan nimi

ASDEX Upgrade -tokamakin nopeiden ionien radanseurantasimulointi magneettisen kareen ja radiaalisähkökentän vaikutuksen alaisena

Käsikirjoituksen päivämäärä 1.4.2008	Korjatun käsikirjoituksen päivämäärä
Väitöstilaisuuden ajankohta 18.8.2008	
☐ Monografia	☑ Yhdistelmäväitöskirja (yhteenveto + erillisartikkelit)

Tiedekunta	Informaatio- ja luonnontieteiden tiedekunta
Laitos	Teknillisen fysiikan laitos
Tutkimusala	Fuusio ja plasmafysiikka
Vastaväittäjä(t)	Prof. Klaus Schöpf
Työn valvoja	Prof. Rainer Salomaa
Työn ohjaaja	PhD Taina Kurki-Suonio

Tiivistelmä

Plasman magneettiseen koossapitoon perustuva tokamak on toistaiseksi lupaavin ratkaisu hallitun fuusion aikaansaamiseksi. Avainkysymyksiä tulevien fuusiolaitteiden kuten ITERin kannalta on kuuman plasman ja kylmien seinämien välinen vuorovaikutus. Hyvän koossapidon toimintatilalle, H-moodille, ovat ominaisia niin kutsutut *reunaleet*, jotka ilmenevät ajoittaisina hiukkas- ja energiaryöppyinä. Äskettäin keksityssä *säyseässä H-moodissa* reunaleet korvautuvat plasman reunan jatkuvalla, kerrannaisista taajuuksista muodostuvalla värähtelyllä. Säyseä H-moodi edellyttää, että käytetään plasmavirtaan nähden vastakkaisesti suunnattuja neutraalisuihkuja, kun taas tavallinen H-moodi saadaan aikaan myötäsuunnatuin neutraalisuihkuin. Neutraalisuihkuionit siis vaikuttavat reunaleiden syntyyn, luultavasti muokkaamalla reuna-alueen stabiilisuutta.

Väitöskirjassa tutkitaan myötä- ja vastakkaissuunnattujen neutraalisuihkujen tuottamien nopeiden ionien käyttäytymistä ASDEX Upgrade -tokamakissa Monte Carlo -radanseurantaohjelmisto ASCOTilla. Tulokseksi saadaan ionien hetkellinen 4-ulotteinen jakauma paikka- ja nopeusavaruudessa sekä häviöistä aiheutuvat seinämäkuormat. Mallinnuksessa on otettu huomioon toroidikenttäkäämien äärellisestä määrästä johtuvan magneettikentän epähomogenian, magneettisen kareen sekä radiaalisähkökentän vaikutus. Neutraalisuihkuionien lisäksi tutkitaan seinämiltä mitatun tritiumin jakauman ja deuterium–deuterium-reaktioissa syntyneiden fuusiotritoneiden vuon välistä vastaavuutta.

Johtuen erisuuntaisesta gradienttiajautumisesta, vastakkaissuunnattujen neutraalisuihkuionien häviöt ovat suurempia kuin myötäsuunnattujen. Tästä seurauksena on suurempi seinäkuorma, mutta myös suurempi nopeiden ionien tiheys reuna-alueella. Lisäksi ionien nopeusjakauma on erilainen. Kareen aiheuttama hiukkasratojen stokastinen diffuusio kasvattaa häviöitä ja seinäkuormia sekä pienentää reunatiheyttä. Sähkökenttä aiheuttaa ratatopologian ja radanleveyden muutoksia: vastakkaissuunnattujen ionien radat kapenevat ja myötäsuunnattujen levenevät. Seurauksena häviöt ja seinäkuormat kasvavat entisestään, mutta silti myös reunatiheys kasvaa. Sähkökenttä aiheuttaa muutoksia myös nopeusjakaumassa. Mallinnettuja 4-ulotteisia jakaumia voidaan jatkossa käyttää säyseän H-moodin alkuperän selvittämiseen analysoimalla erisuuntaisten neutraalisuihkujen vaikutusta reuna-alueen stabiilisuuteen.

Asiasanat	fuusio, tokamak, Monte Carlo -menetelmät, nopeat hiukkaset, ASCOT-simulointiohjelmisto		
ISBN (painettu)	978-951-22-9458-9	ISSN (painettu)	1795-2239
ISBN (pdf)	978-951-22-9459-6	ISSN (pdf)	1795-4584
Kieli	englanti	Sivumäärä	38 + liitteet 80
Julkaisija	Teknillinen korkeakoulu		
Painetun väitöskirjan jakelu	Teknillisen fysiikan laitos, PL 4100, 02015 TKK		
☑ Luettavissa verkossa osoitteessa http://lib.tkk.fi/Diss/2008/isbn9789512294596/			

Acknowledgements

The research presented in this thesis has been carried out at the Laboratory of Advanced Energy Systems at Helsinki University of Technology. It has been an interesting almost-five-year journey into the realm of plasma physics during which I have made many new friends and acquaintances.

I wish to thank my instructor, Dr. Taina Kurki-Suonio, for introducing me to this field of research and for being both my boss and my friend in suitable proportions. I am also thankful to my supervisor, Professor Rainer Salomaa, for encouraging me in my ambitions, both before and after finishing my Master's thesis.

I thank the people of ASDEX Upgrade Team at Max-Planck-Institut für Plasmaphysik for providing me with the background data for the orbit-following simulations. I am particularly grateful to Dr. Wolfgang Suttrop, Dr. Ralph Dux, Dr. Albrecht Stäbler and Dr. Kazuyoshi Sugiyama for all their help in the preparation and analysis of the simulations.

The manuscript was reviewed by Professor Arthur Peeters, University of Warwick, and Dr. Tuomas Tala, Culham Science Centre, Abingdon, Oxfordshire. I thank them for their time and encouraging comments.

A financial grant from the Jenny and Antti Wihuri Foundation is gratefully acknowledged.

This work, supported by the European Communities, under the contract of Association between Association Euratom–Tekes, has been carried out within the framework of the European Fusion Development Agreement. The views and opinions expressed herein do not necessarily reflect those of the European Commission. The computations presented in the thesis have been made with CSC's computing environment. CSC is the Finnish IT centre for science and is owned by the Ministry of Education.

On a less serious note, I wish to thank my friends, co-workers and family for the good times spent in recuperating from the toils of work. You make it worth the while.

Espoo, June 2008

Ville Hynönen

Contents

List of Publications

This thesis consists of an overview and the following publications (ordered by their time of publication) which are referred to in the text by their Roman numerals.

I W. Suttrop, V. Hynönen, T. Kurki-Suonio, P. T. Lang, M. Maraschek, R. Neu, A. Stäbler, G. D. Conway, S. Hacquin, M. Kempenaars, P. J. Lomas, M. F. F. Nave, R. A. Pitts, K.-D. Zastrow, the ASDEX Upgrade team, and contributors to the JET-EFDA workprogramme (2005). Studies of the "Quiescent H-mode" regime in ASDEX Upgrade and JET. *Nuclear Fusion* **45**(7) 721–730.

II V. Hynönen, T. Kurki-Suonio, W. Suttrop, R. Dux, K. Sugiyama, and the ASDEX Upgrade Team (2006). ASCOT simulations of fast particle effects on ASDEX Upgrade edge. In F. De Marco and G. Vlad (editors), *Proceedings of the 33rd European Physical Society Conference on Plasma Physics, Rome, Italy, June 19–23, 2006, Europhysics Conference Abstracts*, vol. 30I, P–2.151 (4 pp). European Physical Society.

III V. Hynönen, T. Kurki-Suonio, W. Suttrop, R. Dux, K. Sugiyama, and the ASDEX Upgrade Team (2007). Surface loads and edge fast ion distribution for co- and counter-injection in ASDEX Upgrade. *Plasma Physics and Controlled Fusion* **49**(2) 151–174.

IV T. Kurki-Suonio, V. Hynönen, T. Ahlgren, K. Nordlund, K. Sugiyama, R. Dux, and the ASDEX Upgrade Team (2007). Fusion tritons and plasma-facing components in a fusion reactor. *Europhysics Letters* **78**(6) 65 002 (6 pp).

V V. Hynönen and T. Kurki-Suonio (2007). Erratum on surface loads and edge fast ion distribution for co- and counter-injection in ASDEX Upgrade. *Plasma Physics and Controlled Fusion* **49**(8) 1345–1347.

VI V. Hynönen, T. Kurki-Suonio, K. Sugiyama, R. Dux, A. Stäbler, T. Ahlgren, K. Nordlund, and the ASDEX Upgrade Team (2007). Fusion tritons and plasma-facing components in a fusion reactor. In P. Gąsior and J. Wołowski (editors), *Proceedings of the 34th European Physical Society Conference on Plasma Physics, Warsaw, Poland, July 2–6, 2007, Europhysics Conference Abstracts*, vol. 31F, P–4.034 (4 pp). European Physical Society.

VII V. Hynönen, T. Kurki-Suonio, W. Suttrop, A. Stäbler, and ASDEX Upgrade Team (2008). Effect of radial electric field and ripple on edge neutral beam ion distribution in ASDEX Upgrade. *Plasma Physics and Controlled Fusion* **50**(3) 035014 (15 pp).

Author's contribution

In **Publication I**, the quiescent H-mode at ASDEX Upgrade and JET tokamaks and its link to magnetohydrodynamic activity called edge harmonic oscillations are studied. Orbit following calculations using the ASCOT code are used to obtain information about the slowing-down distribution of neutral beam ions for co- and counter-injection and the effect of radial electric field on toroidal precession and orbit width of the beam ions.

In **Publications II** and **III**, the slowing-down distribution of co- and counter-injected beam ions and the surface loads caused by them are studied in more detail by ASCOT simulations, taking into account the effects of toroidal ripple and radial electric field. Also the relation between the flux of fusion tritons onto the material surfaces and the measured tritium surface distribution is studied. A programming error affecting the evaluation of collisions in the neutral beam simulations necessitated a corrigendum, **Publication V**, in which a summary of the corrected surface loads is presented. The corrected fast ion distribution results are presented **Publication VII**, focusing on the effect of radial electric field and including its effect on collisionless single-particle orbits.

In **Publication IV**, projections about the accumulation of fusion tritons in a long-pulse or steady-state fusion reactor are made. The results obtained in **Publication III** are presented as a reference about the uneven distribution of fusion tritium on the plasma-facing components. The modelling of the triton flux onto the surfaces is carried on in **Publication VI**.

The author has participated actively in all of the analysis presented in the publications except for the study of the quiescent H-mode and edge harmonic oscillations in **Publication I**, the tritium surface distribution measurements in **Publications III** and **IV**, and the analysis of tritium implantation using the SRIM2003 code in **Publications IV** and **VI**. In particular, all the numerical work related to the ASCOT code – i.e., the simulations as well as the development and application of post-processing tools – has been done by the author. The analysis of the post-processed results, the thinking and toiling, has been done as teamwork.

List of Abbreviations

Abbrev.	Description	See page
ASCOT	Accelerated Simulation of Charged particle Orbits in Tori	4
ASDEX	Axially Symmetric Divertor EXperiment	2
AUG	ASDEX UpGrade	2
CPU	Central Processing Unit	14
CX	Charge eXchange (collision)	9
DD	Deuterium-Deuterium (fusion reaction)	2
DIII-D	Doublet III Big Dee	2
ECRH	Electron Cyclotron Resonance Heating	2
ELM	Edge Localized Mode	1
FLUSH	FLUx Surface Handling (library)	12
FORTRAN	The IBM mathematical FORmula TRANslating system	14
FT-2	Fizicheskii Tokamak-2	8
H-mode	High confinement mode	1
IC	Ion Cyclotron (waves)	8
ICRH	Ion Cyclotron Resonance Heating	2
ITER	International Thermonuclear Experimental Reactor (obsolete)	1
JAERI	Japan Atomic Energy Research Institute	28
JET	Joint European Torus	12
JT-60U	JAERI Tokamak-60U	28
LH	Lower Hybrid (waves)	8
MHD	Magnetohydrodynamic(s)	2
MPI	Message Passing Interface (library)	15
NBI	Neutral Beam Injection	2
NPA	Neutral Particle analyzer	13
OFMC	Orbit-Following Monte Carlo	4
PSL	Photo-Stimulated Luminescence	23
QH-mode	Quiescent H-mode	2
RF	Radio Frequency	2
SI	Le Système International d'Unités	13
SOL	Scrape-Off Layer	9
SOLPS	Scrape-Off Layer Plasma Simulator	10
SPOT	Simulation of Particle Orbits in a Tokamak	4
SRIM	The Stopping and Range of Ions in Matter	ix
TF	Toroidal Field	10

List of Symbols

Symbol	Description	See page
$\blacksquare_{\parallel}$	Component parallel to magnetic field	5
$\blacksquare_{\perp}$	Component perpendicular to magnetic field	5
Δt	Length of time step	7
Ω	Larmor frequency	5
ϵ	Particle energy	7
θ	Poloidal angle (geometrical)	14
μ	Magnetic moment (1st adiabatic invariant)	6
ν	Pitch collision frequency	7
$\nu_{\epsilon,j}$	Energy collision frequency	7
ξ	Particle pitch (pitch angle cosine)	7
ρ	Radial coordinate (related to minor radius)	7
ρ_{pol}	Normalized poloidal radius	10
τ_{B}	Bounce time	6
ψ	Poloidal flux	10
ψ_{axis}	Poloidal flux at the magnetic axis	10
ψ_{sep}	Poloidal flux at the separatrix	10
A_{acc}	Acceleration factor	8
B_θ	Poloidal magnetic field	21
$\boldsymbol{E}_\phi$	Toroidal electric field	8
k_{B}	Boltzmann constant $= 1.3806503 \times 10^{-23}\,\mathrm{J/K}$	7
R	Major radius	10
r	Minor radius	18
r_θ	Poloidal gyroradius	21
r_{L}	Larmor radius	5
T	Plasma temperature	7
$\boldsymbol{v}_{\boldsymbol{E}}$	$\boldsymbol{E}\times\boldsymbol{B}$ drift velocity	5
$\boldsymbol{v}_{\mathrm{gc}}$	Guiding-center velocity	5
$\boldsymbol{v}_{\nabla \boldsymbol{B}}$	Gradient and curvature drift velocity	5
v_{th}	thermal velocity	21

List of Figures

1 Introduction

Fusion in stars keeps the universe rolling, but terrestrially its direct use has begun only recently. Presently, magnetic confinement of plasma inside a tokamak is the most promising form of controlled fusion on Earth. However, a mix of deuterium and tritium producing significant fusion power has so far been used only in a few experiments [1–3]. In the future, ITER will the testbed of real, self-sustained fusion [4].

A key issue for fusion, if not *the* key issue, is the interaction between the hot plasma and the cold material surfaces. In the past, the focus of plasma operation has been more on the core plasma properties, and care has been taken to protect the plasma from the wall. At present, it is instead becoming increasingly important to protect the plasma-facing components from the plasma. Particularly important are the so-called edge localized modes (ELMs) [5–7] which are the earmark of high confinement mode (H-mode) [8] plasmas. ELMs are recurrent, weak instabilities of the edge plasma which manifest themselves as bursts of energy and particles. They may cause very high peak heat loads, but at the same time they conveniently exhaust impurities and control the density.

A plasma discharge in a tokamak can be characterized by its average density, temperature, and confinement time. These quantities appear in the fusion triple product used to assess how close to ignition the plasma is. In the other extreme, a full 6-dimensional, time-evolving distribution function $f(\boldsymbol{r}, \boldsymbol{v}, t)$ can be used to describe the plasma. Most of the time, the useful approach from the modelling point of view lies somewhere in between the two. For steady-state problems, the time dimension can be dropped. The bulk of the plasma can be described by a shifted Maxwellian distribution having a local temperature and density. Due to the concentric flux-surface structure characteristic of toroidal devices, the dependency on the location can often be reduced to one dimension, the minor radius.

In the test particle approach, an ensemble of test particles representing a minority population is simulated on top of a stationary, locally Maxwellian background plasma. The minority population represented by the test particles can, in principle, be any particle distribution (e.g., impurities or neutral particles) so long as it does not perturb the background. If this requirement is not fulfilled, self-consistent modelling of both the minority and the background is required. This would typically involve an iterative process in which the two populations are repeatedly and successively updated.

One interesting minority population is the fast particles [9] which in some form are always present in tokamak experiments. In present experiments, they are primarily produced by external heating – i.e., neutral beam injection (NBI) and radio-frequency (RF) heating. In future experiments starting from ITER, they will be produced in vast quantities in fusion reactions. A small number of fusion tritons are produced in deuterium-deuterium (DD) fusion reactions also in the present experiments.

Fast particles must be confined long enough to transfer their energy to the background and not to cause excessive surface loads. They can also drive or stabilize magnetohydrodynamic (MHD) instabilities. Conversely, certain MHD phenomena can deteriorate the confinement of fast particles. For instance, the fishbone instability [10, 11] is driven by neutral beam ions, and the toroidal Alfvén eigenmodes can be destabilized by fusion alpha particles [12] or by externally heated ions [13, 14]. The sawtooth oscillations, on the other hand, can be stabilized by fast ions [15]. An example of the adverse effect of MHD instabilities on fast particles is the class of instabilities known as the neoclassical tearing modes which can increase fast ion losses and modulate them by the frequency of the mode [16].

The above examples of instabilities are bulk plasma MHD phenomena, but it is becoming apparent that fast ions may play a role also in the stability of the plasma egde and thus affect ELMs. One indication of this is the so-called quiescent H-mode (QH-mode) [17] which is ELM-free, but with stationary density and impurity content. The density control in the QH-mode is effected by an MHD activity called edge harmonic oscillations which enhance the particle transport but leave the energy transport unaffected. So far, QH-mode has been obtained only by using counter-injected neutral beams which produce a different kind of edge fast ion distribution than co-injected beams.

Quiescent H-mode was initially discovered at DIII-D [18] (General Atomics, San Diego, CA, USA), but it has later been obtained also in other tokamaks, including ASDEX Upgrade (AUG) at Max-Plank-Institut für Plasmaphysik in Garching, Germany [19]. ASDEX Upgrade is a medium-size divertor tokamak [20] with a substantial amount of installed heating power relative to its size. Consequently, the surface loads in AUG are in ITER-relevant regime. The total installed heating power, 30.6 MW, consist of 20 MW NBI, 8 MW of ion cyclotron resonance heating (ICRH), and 2.6 MW of electron cyclotron resonance heating (ECRH). The maximum absorbed NBI power varies between 18 MW and 20 MW, depending on the shine-through and first-orbit losses. All of ECRH is always coupled into plasma,

and for the ICRH, 5.6 MW is achieved routinely.

In this thesis, the fast ion losses and the edge fast ion distribution in H- and QH-mode of ASDEX Uprade are studied using the orbit-following Monte Carlo code ASCOT. Also the surface distribution of tritium created in DD fusion reactions is addressed. The ASCOT code is introduced in chapter 2. The behaviour of collisionless particles, understanding of which is necessary for the analysis of full simulations, is discussed in chapter 3. Results from the full simulations, presented in detail in **Publications I–VII**, are summarized in chapter 4. Finally, chapter 5 contains discussion on the obtained results and possible future work.

2 The simulation model

The guiding-center orbit-following Monte Carlo code ASCOT [21–23] is intended for studies of neoclassical charged particle behaviour in tokamaks and stellarators. A number of similar orbit-following codes have been developed, such as the code by Tani *et al.*[1] [24], ORBIT [25] and ORBITX [26], FAFNER [27–29], the fast ion module NUBEAM in the National Transport Code Collaboration library [30], GOURDON [31], and SPOT [32]. ASCOT follows the guiding-center orbits of test particles determined by the $\boldsymbol{E}\times\boldsymbol{B}$, gradient, and curvature drifts in a realistic 2D or 3D magnetic background. A radial electric field can be imported into the code as a radial profile or it can be represented in a simple analytical form, such as polynomial or a step function. Collisions and other particle-background interactions are modelled by Monte Carlo operators derived from the Fokker-Planck equation. The test particles are followed until a prescribed end criterion is reached, and information about each orbit is collected into various diagnostics which can be further analyzed after completing the simulation.

ASCOT has been in a state of continuous, although perhaps somewhat intermittent, development since 1991. The following sections describe the present state of ASCOT focusing on the aspects directly related to the thesis and recent development of the code. Some tools providing input data for ASCOT are also discussed because they are an essential part of the whole simulation process. The author has participated particularly in the code development related to the magnetic field (see section 2.2.2) and in the modernization of the distribution diagnostics described in section 2.3.1.

2.1 Orbit-following

2.1.1 Equation of motion

In full generality, the motion of a charged particle in an electromagnetic field is governed by the (non-relativistic) Lorentz force

$$\boldsymbol{F} = m\frac{\mathrm{d}\boldsymbol{v}}{\mathrm{d}t} = q(\boldsymbol{E} + \boldsymbol{v}\times\boldsymbol{B}). \tag{2.1}$$

In a constant, uniform magnetic field $\boldsymbol{B}$ this will result in a helical motion consisting of a constant velocity parallel to the magnetic field and a rapid gyration around a

[1] The code by Tani *et al.* [24] is nowadays often referred to as OFMC (Orbit-Following Monte Carlo), although strictly speaking that is the name of a group of codes.

magnetic field line arising from the $\boldsymbol{v} \times \boldsymbol{B}$-term. The frequency and radius of the gyration are $\Omega = qB/m$ (Larmor frequency) and $r_\mathrm{L} = v_\perp / |\Omega|$ (Larmor radius), where $v_\perp$ is the velocity component perpendicular to the magnetic field. In a more general magnetic field with a gradient and curvature, a drift velocity

$$\boldsymbol{v}_{\nabla \boldsymbol{B}} = \frac{v^2 + v_\parallel^2}{2\Omega} \frac{\boldsymbol{B} \times \nabla B}{B^2} \tag{2.2}$$

is superposed upon the parallel velocity $v_\parallel$ and the gyromotion. Another drift,

$$\boldsymbol{v}_{\boldsymbol{E}} = \frac{\boldsymbol{E} \times \boldsymbol{B}}{B^2}, \tag{2.3}$$

arises in the presence of a constant, uniform eletric field $\boldsymbol{E}$. In addition to the drift, an eletric field causes acceleration in the parallel direction.

Due to the very short time scales and oscillatory nature of the gyromotion, it is computationally impractical and numerically challenging to integrate the particle motion directly from the Lorentz-force. In a rapidly varying or highly nonuniform magnetic field there would be no alternative, but under the steady-state or slowly changing conditions of magnetic confinement plasma experiments the guiding-center approximation can be used. More precisely, the Larmor radius must be small compared to the scale length of the magnetic field and the Larmor frequency must be large compared to the rate of change of the magnetic field, i.e.,

$$\frac{r_\mathrm{L} |\nabla B|}{B} \ll 1 \tag{2.4}$$

$$\frac{1}{|\Omega| B} \frac{\mathrm{d}B}{\mathrm{d}t} \ll 1. \tag{2.5}$$

In such a situation the magnetic field can be linearized around the guiding-center location and the particle velocity averaged over the Larmor period yielding the guiding-center equation of motion

$$\boldsymbol{v}_\mathrm{gc} = \frac{v_\parallel \boldsymbol{B}}{B} + \frac{v^2 + v_\parallel^2}{2\Omega} \frac{\boldsymbol{B} \times \nabla B}{B^2} + \frac{\boldsymbol{E} \times \boldsymbol{B}}{B^2}, \tag{2.6}$$

where each variable is now evaluated at the guiding-center position. The first term on the right-hand side is the fast parallel motion and the two latter terms are the drifts mentioned above. The acceleration along the magnetic field is given by

$$\frac{\mathrm{d}v_\parallel}{\mathrm{d}t} = \frac{q}{m} \frac{\boldsymbol{E} \cdot \boldsymbol{B}}{B} - \frac{\mu}{m} \frac{B \cdot \nabla B}{B}, \tag{2.7}$$

where the first term on the right-hand side corresponds to acceleration due to parallel electric field $E_\parallel = \boldsymbol{E} \cdot \boldsymbol{B}/B$,and the second to the mirror force which can reflect particles moving into a magnetic field of increasing magnitude (see also section 3.1) [33].

The quantity denoted by

$$\mu = \frac{mv_\perp^2}{2B} \tag{2.8}$$

is the magnetic moment which is an adiabatic invariant.

2.1.2 Orbit integration

The equations (2.6) and (2.7) can be solved in ASCOT either in Cartesian coordinates or in field-aligned magnetic coordinates by A. H. Boozer [34, 35] in which the Hamiltonian equations of motion presented by White and Chance are used [25]. The Boozer coordinate system, being specifically developed for toroidal systems, is intrinsically more accurate than the general-purpose Cartesian system, but presently it can only be used in an axisymmetric magnetic field, i.e., without toroidal ripple (see section 2.2). For this reason, in the work related to the thesis only the Cartesian coordinate system has been used. Boozer coordinate system is also restricted to the region where the magnetic surfaces are closed, i.e., inside the separatrix.

Whenever Cartesian coordinates are in use, a 5^{th} order Runge-Kutta adapted from the variable-order Runge-Kutta by Cash and Karp [36] is used for orbit integration. After completing the time step and obtaining the new guiding-center location and parallel velocity, the new perpendicular velocity is solved from the invariance of the magnetic moment, i.e., from equation (2.8). The new particle energy is then obtained from the velocities. The energy conservation is, thus, not explicit in the code, and any numerical errors in the orbit integration will be visible as nonphysical drifts of energy. Such drifts can be prevented to a degree by monitoring the truncation error of the Runge-Kutta integration step and by reducing the time step if the error exceeds a prescribed tolerance, but there are also smoothness requirements for the magnetic background (see section 2.2). When the Boozer coordinate system is used, however, a 4^{th} order Runge-Kutta without any error monitoring has been found satisfactory both in accuracy and, especially, speed.

The initial time step is chosen such that it is much smaller than the bounce time τ_B, the time it takes for a particle to complete one revolution or bounce in the poloidal plane (see section 3.1). The default time step in an axisymmetric magnetic field is $\tau_\text{B}/25$, but there are a number of limiting factors, such as toroidal ripple and various interaction time scales, which are taken into account when deciding the default time step. The default time step is updated once each orbit.

2.1.3 Collisions and other interactions

Interactions between test particles and background are evaluated between orbit-integration time steps. They are modelled by Monte Carlo operators based on binomial distribution, except for the effect of a constant toroidal electric which is deterministic. In an axisymmetric magnetic field the time scales of collisions and other interactions can be accelerated with respect to the orbit-following time scale, greatly reducing the simulation time.

The Coulomb collision Monte Carlo operators are derived from the Lorentz and Fokker-Planck collision operators using Rosenbluth potentials [37, 38]. Their effect on particle pitch ξ and energy ϵ is

$$\Delta\xi = -\nu\xi\Delta t + \delta_1 \left[(1-\xi^2)\nu\,\Delta t\right]^{1/2}, \tag{2.9}$$

$$\Delta\epsilon = -\sum_j 2\nu_{\epsilon,j}\Delta t \left[\epsilon - \left(\frac{3}{2} + \frac{\epsilon}{\nu_{\epsilon,j}}\frac{\mathrm{d}\nu_{\epsilon,j}}{\mathrm{d}\epsilon}\right) k_\mathrm{B}T_j\right] + \delta_2 \left(\sum_j 2k_\mathrm{B}T_j\epsilon\,\nu_{\epsilon,j}\,\Delta t\right)^{1/2}, \tag{2.10}$$

where ν is the pitch collision frequency, Δt is the length of the time step, $\nu_{\epsilon,j}$ and T_j, respectively, are the energy collision frequency and temperature for plasma species j, k_B is the Boltzmann constant, and $\delta_{1,2}$ are uniformly distributed random signs (± 1). The first terms on the right-hand sides of the equations are the deterministic ones which drive particle pitch towards zero and energy towards the local temperature. The seconds terms are the stochastic ones which make, given enough time and evaluations of the operators, the shape and width of the distribution: uniform distribution in $[-1, 1]$ for the pitch and Maxwell-Boltzmann distribution for the energy. In order to have a good representation of the Lorentz and Fokker-Planck operators, both $\nu\Delta t$ and $\nu_\epsilon\Delta t$ must be much less than one. These requirements set an upper limit for the time step which is taken into account in ASCOT. For cases where relativistic effects must be taken into account, energy operator derived from the linearized, relativistic Balescu-Lenard collision operator [39, 40] for nonrelativistic, Maxwellian background is used. The relativistic operator reduces to (2.10) at non-relativistic energies.

The effects of anomalous radial diffusion can be modelled by a simple Monte Carlo diffusion operator with a diffusion coefficient D [41, 42]. The change in the radial coordinate ρ during a time step Δt is

$$\Delta\rho = D\,\frac{\partial A}{\partial\rho}\,\frac{\Delta t}{A} + \delta_3\sqrt{2D\Delta t}, \tag{2.11}$$

where A is the area of the flux surface and δ_3 is a random sign as above. Initially the diffusion coefficient D was implemented as constant, but it has been recently updated to have the following dependency on energy:

$$D = D(\rho, \epsilon) = D_0(\rho) \frac{\epsilon_0}{\epsilon_0 + \epsilon}. \tag{2.12}$$

Here, ϵ_0 is a parameter, typically of the order of 10 times the local ion temperature, and $D_0(\rho)$ is a simple step function having two values on each side of some ρ_0. This energy dependency is motivated by the recent observation that for reasonable parameters, anomalous diffusion of thermal and suprathermal particles can be similar [43].

Although the effect of an electric field is taken into account in the equations of motion (2.6) and (2.7), there exists a separate model for the effect of a toroidal electric field $\boldsymbol{E}_\phi$ [21, 41]. The change in particle energy during a time step Δt is

$$\Delta\epsilon = q(\boldsymbol{v} \cdot \boldsymbol{E}_\phi)\Delta t, \tag{2.13}$$

where $\boldsymbol{v}$ is the average velocity vector during the time step.

Monte Carlo operators based on phenomenological models of interactions between test particles and radiofrequency waves exist in ASCOT. The operator describing the effect of lower hybrid (LH) on ions and electrons is derived from the wave diffusion term of the diffusion equation for the test particle distribution [37]. The ion cyclotron (IC) wave operators on perpendicular velocity and toroidal momentum are derived from the quasilinear diffusion model of IC heating [44]. Lately these models and operators have been in little use, but earlier they have been used to study the effect of LH waves on electrons and alpha particles [22, 42, 45], and the interaction of test ions with IC waves [46]. They were also used in simulations of internal transport barrier formation in the FT-2 (Fizicheskii Tokamak-2) tokamak at the Ioffe Institute in St. Petersburg, Russia [47].

For fast, superthermal particles the time scales of most interactions are much longer than the bounce time τ_B. This means that a large number of practically identical guiding-center orbits must be completed to see a noticeable change in the particle parameters. The problem can be alleviated by accelerating the particle interactions and thus letting each followed guiding-center orbit represent many orbits. This is implemented in ASCOT by multiplying the time step Δt by a variable acceleration factor A_acc while evaluating the particle interactions. The method is based on the periodicity of orbits in the absence of interactions [48]. Care must be taken, however, so as not to enhance the collision rate too much to cause artificial changes in the orbit

topology, e.g., from marginally trapped to passing, which would reduce the likelihood of orbit loss. Furthermore, acceleration becomes impossible in a 3D magnetic field in the presence of toroidal ripple because the collisionless orbits are no longer periodic. Selective acceleration of only passing orbits has been experimented, though, because the stochastic diffusion caused by the ripple affects mostly trapped orbits (see also section 3.2).

A double precision version of the pseudorandom number generator proposed by Marsaglia *et al.* [49] is used in ASCOT to produce the random signs required for the Monte Carlo operators. The collision operators can also be cast in a form in which normally distributed random numbers are used instead of random signs. This approach has been used in the code by Tani *et al.* [24].

In addition to the relatively simple interactions listed above, there are also other, more complex models in ASCOT. The models for momentum- and energy-conserving binary collisions [50, 51] and self-consistent radial electric field [52, 53] involve the use of so-called global time steps during which all test particles in the simulation ensemble are advanced several bounce times. After each global time step, the binary collisions are evaluated and the radial electric field is updated. These models are used in simulations of the thermal bulk plasma, but they are less applicable for minority fast ion simulations. A charge-exchange (CX) collision model based on the collisionality formula of Cornelis *et al.* [54, 55] can be used to account for the effect of neutral atoms and molecules on the test particles. After the collision the test particle is followed as neutral until it is re-ionized or lost. Presently the model works only for hydrogen isotopes because cross sections for other test particles species have not been implemented.

2.2 Background data

Although it is possible to use analytical models to represent the magnetic field and plasma profiles, at present the use of experimental backgrounds is much more common. Small auxiliary programs are used to retrieve the data from a database and process it to form suitable for ASCOT. More and more often the toroidal ripple is included in the magnetic background, either as first couple of terms of the Fourier expansion in the toroidal direction, or directly as 3D arrays. The plasma background is still mostly given in 1D, i.e., as radial profiles, but outside the separatrix a 2D scrape-off layer background (SOL) can be used. The extension of the 2D SOL background to cover also inner part of the plasma is straightforward. Instead of the

self-consistent radial electric field model discussed in previous section, a stationary E_r profile can be used. A 2D or 3D model of the wall and divertor is used to mark the limits of the simulation domain. For NBI simulations the test particle ensemble is created using an experiment-specific specialist code.

2.2.1 Plasma background

The plasma background consists of electron and ion densities and temperatures. Inside the separatric they are given as a function of the radial coordinate ρ, which is most often the normalized poloidal radius

$$\rho_\mathrm{pol} = \left(\frac{\psi - \psi_\mathrm{axis}}{\psi_\mathrm{sep} - \psi_\mathrm{axis}} \right)^{1/2}, \tag{2.14}$$

where ψ is the poloidal flux, and ψ_axis and ψ_sep are its values at the magnetic axis and separatrix, respectively. In principle any other reasonable radial coordinate could be used, e.g. normalized volume, or normalized toroidal flux instead of poloidal flux. Outside the separatrix the density and temperature are no longer flux functions but they can be given as functions of R and z instead. The same could also be done inside the separatrix, but so far there has been no need. It is also more efficient to use radial profiles because interpolation is faster in 1D than in 2D.

There can be several ion species in the plasma, but in the present implementation all species have the same shape of the density profile which is scaled according to the plasma composition and requirement for quasi-neutrality. There is ongoing development to remove this restriction and allow independent main ion and impurity densities, although this means that it will be up to the user to ascertain the quasineutrality of the composition.

The plasma profiles are measured ones, although some user intervention by an experimentalist is required to oversee the fitting of the noisy measurement data into numerically more useful parametrized forms. For the 2D SOL background, a delicate and time-consuming simulation with a specialist code such as SOLPS (Scrape-Off Layer Plasma Simulator) [56] is required. Consequently such data are not routinely available which is the reason why a vacuum SOL background is most often used.

2.2.2 Magnetic data

The magnetic background consist of two parts: the vacuum field created by the toroidal field (TF) coils, and the equilibrium induced by the plasma current. The

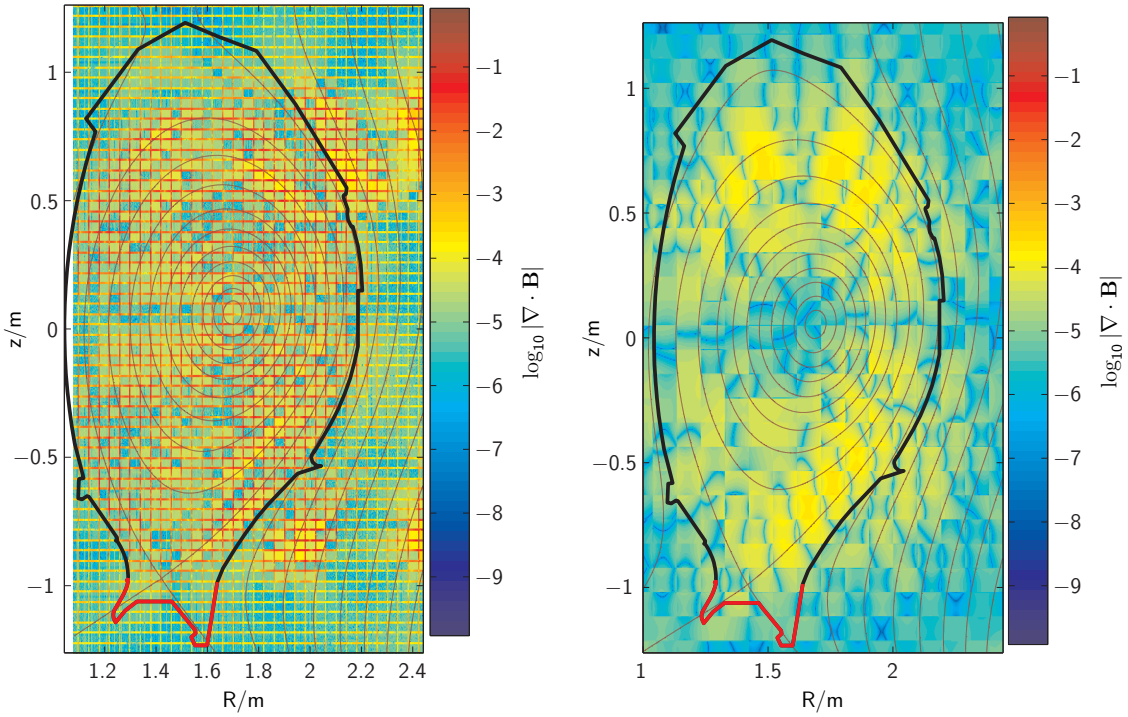

(a) Quadratic (KK-routines) (b) Cubic (splines)

Figure 2.1: Comparison of $|\nabla \cdot \boldsymbol{B}|$ on logarithmic scale for (a) quadratic, and (b) cubic fit of the poloidal flux. The divergence is calculated by second-order finite differences. The grid-like structure in figure (a) originates from the discontinuities of the first derivatives of the magnetic field components. In figure (b) the result is much smoother, although the figure is still divided into panes indicating the knots used in the spline fit.

vacuum field can be further subdivided into an ideal, axisymmetric part without any poloidal components, and a 3D perturbation, the toroidal ripple, arising from the finite number of TF coils. Ideally the ripple is periodic, but in practice local, nonperiodic perturbations are possible. The equilibrium field is mainly poloidal, but a small dia- or paramagnetic contribution to the toroidal component is also present. Generally the equilibrium is 3D just like the vacuum field, but for tokamaks it can be considered to be axisymmetric.

For ASCOT simulations, the equilibrium obtained by solving the Grad-Shafranov equation [33] and the ideal vacuum field is extracted from an experimental database. However, the poloidal flux $\psi(R, z)$ obtained directly from an equilibrium solver is typically not smooth enough to be used in a simulation. Therefore, a least-squares fit by bicubic splines is used to smooth the poloidal flux before it is differentiated to obtain the poloidal magnetic field components. For JET tokamak (Joint European

Torus) at Culham Science Center in Oxfordshire, UK, this is done automatically by the FLUSH library [57], but the KK-library routines [58] used at AUG use quadratic fitting. Consequently, the first derivatives of the poloidal magnetic field components are discontinuous. This is illustrated in figure 2.1 (a) in which the absolute value of $\nabla \cdot \boldsymbol{B}$ on a logarithmic scale is shown for poloidal magnetic field components obtained using the KK-library routines. The non-smooth magnetic background used to be a problem until the program used to retrieve the plasma and magnetic data from the AUG database was modified to use the spline fit procedure described in the FLUSH manual [57]. The divergence of a magnetic background obtained by using splines is illustrated in figure 2.1 (b).

A ripple model of the form

$$B_R(R,\phi,z) = B_{R,0} + A_1 B_{R,1} \sin(N_{\mathrm{coil}}\phi/2) + A_2 B_{R,2} \sin(N_{\mathrm{coil}}\phi), \tag{2.15}$$

$$B_z(R,\phi,z) = B_{z,0} + A_1 B_{z,1} \sin(N_{\mathrm{coil}}\phi/2) + A_2 B_{z,2} \sin(N_{\mathrm{coil}}\phi), \tag{2.16}$$

$$B_\phi(R,\phi,z) = B_{\phi,0} + A_1 B_{\phi,1} \cos(N_{\mathrm{coil}}\phi/2) + A_2 B_{\phi,2} \cos(N_{\mathrm{coil}}\phi). \tag{2.17}$$

was implemented into ASCOT in order to simulate JET ripple experiments in planning at the time [59] (see also **Publication III**). For JET applications, the parameters $A_{1,2}$ depend on the currents in even- and odd-numbered TF coils. In normal operation of JET and other tokamaks, however, the coil currents are equal and the first order (or halfth order, if the ripple period is concerned) terms cancel yielding $A_1 = 0$ and $A_2 = 1$. The 0^{th} order terms $B_{\blacksquare,0} = B_{\blacksquare,0}(R,z)$ form the axisymmetric background discussed above, and the perturbative terms $B_{\blacksquare,1,2} = B_{\blacksquare,1,2}(R,z)$ are obtained from vacuum field calculations.

Recently, a fully three-dimensional magnetic field has been implemented in order to simulate fast ion losses in ITER [60]. In the new model, the magnetic field consist of at most two toroidal sectors having identical shape. These building blocks are copied around the torus, and if necessary, they can be mirrored symmetrically or antisymmetrically. The periodic ripple can be represented with one sector, and the second one can be used for a local perturbation, such as the test blanket modules in ITER. The size of a single sector and the number of grid points in it are limited only by the amount of available memory, leaving the possibility to make one "sector" cover the entire torus.

2.2.3 Other input data

A radial electric field can be imported into ASCOT as a radial profile, or, alternatively, there are two simple functional forms for representing it: a 2-valued step function

(constant E_r between ρ node points), or a cubic polynomial fitted to given extremum points and values. Since E_r is not a flux function, but electric potential is, in all three reprentations the radial electric field is inputted as the derivative of the potential V with respect to ρ, $\mathrm{d}V/\mathrm{d}\rho$. The value of E_r in SI units is obtained by scaling by the local value of $|\nabla\rho|^{-1}$.

In 2D, the wall and divertor structures are represented as a closed contour which is obtained as a list of points (vertices) in (R, z) from experimental database. A simple test based on the winding number (number of times a closed curve encircles a point) is used to check whether a test particle is inside the wall. A 3D wall representation based on planar triangular elements has recently been developed hand in hand with the 3D magnetic field model discussed above. The collisions of test particles with the wall are tested with a ray-polygon intersection algorithm adapted for this purpose [61].

In some cases, especially for NBI simulations, the test particle ensemble is created using experiment-specific specialist codes such as FAFNER at ASDEX Upgrade or PENCIL at JET [62]. A simple NBI initialization model has been implemented into ASCOT as well, but typically the actual geometry of beam components is too complicated to be represented in the simplified form used in the model. For this reason, and because the detailed geometry information is not necessarily available, the use of a specialist code is recommendable.

2.3 Diagnostics

ASCOT follows test particles, each of which represents a large number real particles, typically of the order of 10^{16} or more. Each particle is followed until it leaves the region of space which is of interest in a particular simulation. This can happen both in the configuration space (e.g. losses) and in the velocity space (thermalization) (see **Publication III** for details about NBI simulations). During the simulation, information about the movement of test particles is collected into number of diagnostics. Particle density, radial and parallel currents, power deposition and torque are recorded into different distributions in at most 5 dimensions, including the velocity and time dimensions. The final location and other relevant quantities at the final location are always part of the output, and if required, all points of the particle orbit can also be included. A number of log files and summaries provide information about the functioning of the code. Most of the diagnostics do not have a counterpart in the real world, except for the neutral particle analyzer (NPA) model which

attempts to match its physical equivalent as closely as possible.

2.3.1 Distributions

Information about each time step, including both the orbit integration and effects of collisions and other interactions discussed above, is collected into distributions. The region of interest in the phase space is divided into uniformly spaced cells in the relevant coordinates, including time. The coordinates typically used are normalized poloidal radius ρ_{pol} and poloidal angle θ or (R, z) in the configuration space, and $(v_{\parallel}, v_{\perp})$ or (ϵ, ξ) in the velocity space. The contribution from each time step is accumulated into the cells the test particle has visited. The accumulated quantity depends on the type of distribution:

phase space densities — the time test particles spend in each cell
poloidal and toroidal velocity — velocity
parallel current — velocity multiplied by charge
radial current and torque — radial displacement
power deposition — change in particle energy due to collisions and other interactions
fusion reaction rate — number of fusion reactions.

The accumulated quantity is multiplied by the test particle weight and, if acceleration of interaction time scales is used, also by the acceleration factor. However, for radial current densities, which in essence measure the net radial displacement, the acceleration must not be included.

All constant factors, such as division by the phase space cell volume, are taken into account in post-processing after the simulation in order to save CPU (Central Processing Unit) time. Until recently, most of the distributions were qualitative, i.e., they were not in physical units. Since then, the implementation of the distributions has been rewritten and modernized into FORTRAN 90. Presently, all distribution are in physical units. For details about the normalizations necessary to convert the accumulated quantity into physical units, see appendix A.

2.3.2 Orbits and losses

For studies of single-particle behaviour, the orbit of each test particle can optionally be outputted. The time resolution can be decreased from the default in which all integration time steps are included. In addition to particle location, the time

evolution of several other quantities, such as energy, particle pitch, and canonical toroidal momentum, is included. Even if output of the orbit data is disabled, the number of trapped and untrapped orbits undergone by each particle and the average bounce time are included in one of the log files.

The final location of test particles, together with other relevant quantities, is always included in the output. The losses onto divertor and wall are put into a separate file which can later be postprocessed in, e.g., Matlab to obtain surface loads and other derivative data.

2.3.3 Logs and summaries

The following log files are written for each simulation (see also examples in appendix B):

console — Log of the initialization procedures before the actual simulation is commenced

console_p — Test particle specific and cumulative CPU times

logfile_p — Number of trapped and untrapped orbits, average bounce time, simulation and CPU time

summary — breakdown of test particle final states (thermalized/lost), total resource consumption (CPU time, no. of time steps & orbits), average simulated time & confinement time

If the simulation has been parallelized using the MPI library, the files are written for each process. Additionally, the summary file is written also for the complete simulation. Although only the number of trapped/untrapped and the bounce time are physical quantities, the log files are nevertheless vital because many problem situations can be discovered and frequently even solved by monitoring them.

2.3.4 NPA-model

The original NPA-model in ASCOT has been used for qualitative spectroscopy of neutral particles emitted from the plasma [63]. In 2006, a quantitative benchmark against NPA measurements from several AUG discharges was performed [64]. Although the model did reproduce many of the gross features of the measured spectra, the observed differences warranted a complete review and upgrade of the model.

The model was improved to give the energy-resolved neutral particle flux in SI-units. The NPA source rate is based on parametrized CX reaction rate and mean

free path [65], and the description of NPA geometry closely resembles that of ASDEX Upgrade. However, in order to improve the signal-to-noise ratio, the detector replicated is around the torus. Another geometrical factor is the phase of the gyromotion prior to neutralization: only ions neutralized in the correct phase angle are directed towards the detector. Geometry-based coefficient are used to compensate for these effects and scale the NPA signal to its SI-value. Following the upgrade, the agreement between the model and experiment has been greatly improved.

3 Collisionless orbits

It is usually a valid assumption that fast particles interact only with the thermal background, making a neutral beam simulation a linear operation on individual test particles. For this reason it is instructive to consider the single-particle behaviour before (and after) tackling full simulations. In the absence of collisions, the different orbit topologies arise from the interplay of guiding-center drifts and the mirror force (see equations (2.6) and (2.7)). Toroidal ripple destroys the periodicity of collisionless orbits leading to stochastic diffusion. It also creates local wells to the magnetic field strength along the field line causing ripple well losses. A radial electric field can change the orbit width, the toroidal precession of the orbit, and the duration of inner and outer legs of a trapped orbit. In the extreme case, the entire orbit topology can change. The orbit topologies and E_r-induced orbit transitions of co- and counter-injected neutral beam ions are discussed in **Publication VII**. For discussion about effects of a constant radial electric field on orbit width and toroidal precession, see **Publication I**.

3.1 Orbit topologies

Since the magnetic field is higher on the inner side of the torus, particles having too small parallel velocity are reflected before the maximum magnetic field strength along the field line is reached. The orbit of such *trapped* particles is a combination of vertical gradient drift and alternating parallel motion along the field line, and the image of a trapped orbit projected into the poloidal plane typically resembles a banana. Particles that are not reflected are called *passing* and can be further divided into co-passing and counter-passing according to the sign of parallel velocity. Passing orbits encircling the magnetic axis and trapped orbits not encircling the magnetic axis are called *standard orbits*. In between the two groups are the so-called *pinch orbits*. [66]

Since the combined gradient and curvature drift depends on the velocity, very energetic ions, such as fusion alphas, can drift up or down to the midplane while staying on one side (left or right) of the magnetic axis. In such a case the particle is not reflected but it is nevertheless confined to either side of the poloidal plane. It is therefore toroidally passing but poloidally trapped, and the corresponding orbit is called a *potato orbit* according to its characteristic shape. Trapped orbits that do encircle the magnetic axis are sometimes called *kidney* orbits. In the limit of

reducing the orbit width, the potato orbit becomes a *stagnation orbit*. [66]

In the context of neutral beams, if immediately following the ionization the direction of the gradient drift is inwards in minor radius, the orbit is called *well-confined*. It can be shown that this is always the case for co-injected ions. In the opposite case, e.g., for counter-injected NBI ions, the particle might be called *ill-confined*, but this term is not widely used. If a counter-injected beam particle is ionized close enough to the separatrix, its ill-confined orbit can intersect the wall resulting in *direct orbit loss*.

The time it takes to complete one orbit, i.e., the time in which the projection of the orbit into the poloidal plane closes on itself, is called *bounce time* τ_B. The toroidal drift frequency or the *toroidal precession* is defined as the bounce-averaged value of $\dot{\phi}$,

$$\left\langle \dot{\phi} \right\rangle = \frac{1}{\tau_\mathrm{B}} \oint \dot{\phi} \mathrm{d}t. \tag{3.1}$$

For banana orbits, this is equal to $\Delta\phi/\tau_\mathrm{B}$, where $\Delta\phi$ is the displacement of a banana tip in toroidal angle during one bounce time.

3.2 Ripple trapping and stochastic diffusion

The magnetic field of an ideal tokamak would be axisymmetric, but in reality the number of TF coils is finite leading to toroidal ripple. For spherical cross section and N coils, the toroidal component of the vacuum magnetic field can be represented by

$$B_\phi = B_{\phi,0} \frac{R0}{R_0} R_0 + r\cos\theta(1 - \delta(r,\theta)\cos N\phi), \tag{3.2}$$

where r is the minor radius and R_0 the major radius at the magnetic axis. In certain regions of the poloidal plane this leads to local minima, *ripple wells*, in the magnetic field strength along the field line. An example of the ripple magnitude δ and the ripple-well region is shown in figure 3.1.

In a manner similar to the global trapping discussed above, particles having low parallel velocity can become locally trapped in these ripple wells. Such *ripple-trapped* particles are subsequently lost due to the vertical gradient drift. Ripple-trapping occurs for trapped particles with banana tips inside the edge of the ripple-well region or near its edge. For thermal particles, ripple-trapping results in increased transport via collisional ripple diffusion [67] but for sufficiently energetic particles, which do not suffer a collision before being lost, ripple wells represent a loss cone [68]. Processes feeding particles into this loss cone are

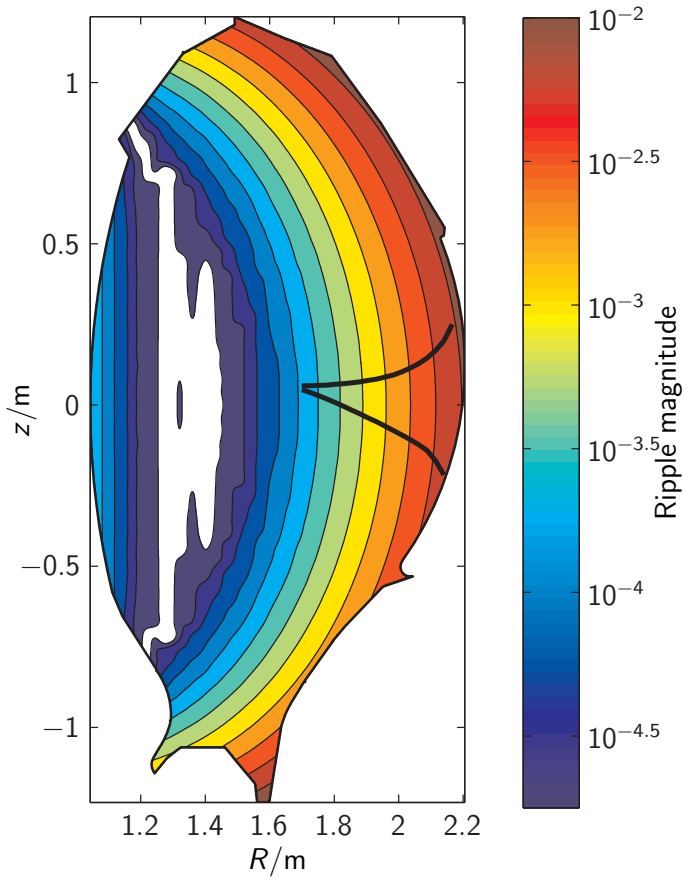

Figure 3.1: Contour plot of the ripple magnitude ($= \delta = (B_{\phi,\max} - B_{\phi,\min})/(B_{\phi,\max} + B_{\phi,\min})$) *of the ASDEX Upgrade vacuum field. The ripple-well region is indicated in the figure by the thick lines. In the white region around* $R \approx 1.3\,\mathrm{m}$*, the ripple magnitude is below the color scale.*

(i) pitch-angle scattering,

(ii) ripple-transport of banana particles,

(iii) acceleration by radio-frequency waves,

(iv) neutral beam injection.

Outside the ripple-well region, the effect of ripple is limited to modification of banana orbits through changes in particle pitch under the conservation of magnetic moment. These variations cancel for passing orbits, but they are significant enough to move the turning point for successive banana bounces and destroy the closure of the orbit. For small displacements, this leads to periodic motion of the banana tips determined by the periodicities of the ripple and toroidal precession. This does not in itself lead

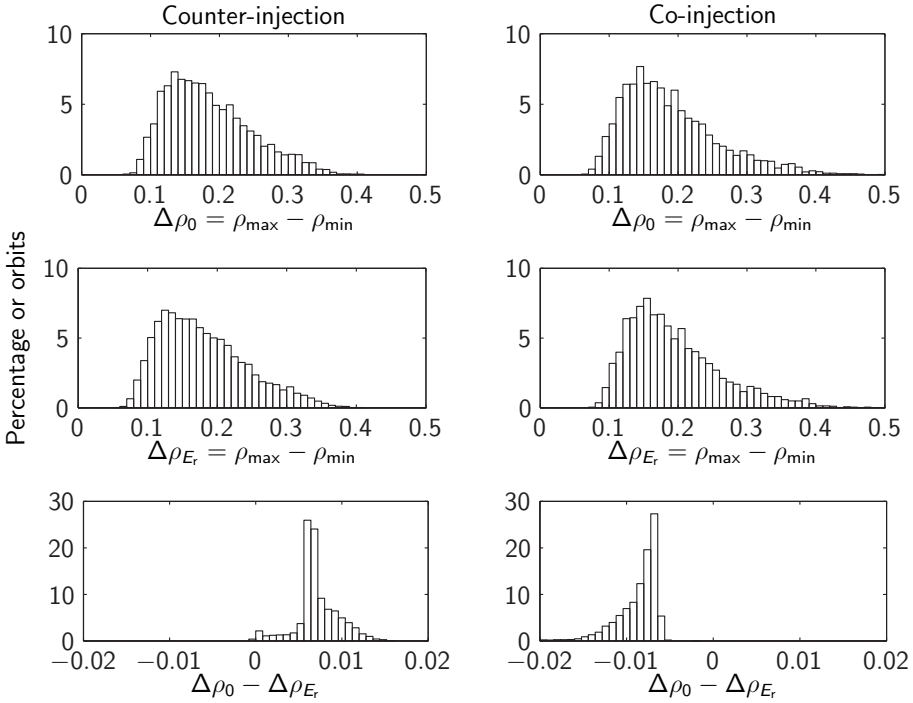

Figure 3.2: Top and middle row: histogram of banana orbit width $\Delta\rho$ with and without radial electric field for 60 keV co- and counter-injected neutral beam ions. Bottom row: histogram of the difference in orbit width with and without E_r. For counter-injection, the orbit width is consistently reduced by the radial electric field, and the converse happens for co-injection.

to losses except when collisions de-correlate successive steps. With stronger ripple, the displacement itself can de-correlate the orbit, leading to stochastization of the motion of banana tips by period doubling. This route to chaos can be analyzed by means of the so-called Chirikov parameter which describes the strength of de-correlation. [69–71]

For fast particles, the non-collisional effects of ripple, ripple trapping and stochastization of the orbit, are more important than the collisional ones. Both lead to increased losses which can be highly localized on the in-vessel wall.

3.3 E_r-induced orbit transitions

The effect of a radial electric field on standard orbits is conventionally thought to be mainly the orbit squeezing or widening in an inhomogeneous E_r. This is expressed

by the squeezing parameter S defined as [72]

$$S = 1 - \frac{r_\theta}{B_\theta v_{\mathrm{th}}} \frac{\mathrm{d}E_\mathrm{r}}{\mathrm{d}r}, \tag{3.3}$$

where $r_\theta = mv_\perp/(qB_\theta)$ is the poloidal gyroradius, B_θ the poloidal magnetic field, and $v_{\mathrm{th}} = \sqrt{k_\mathrm{B}T/m}$ the thermal velocity. The effective poloidal gyroradius is then

$$\hat{r}_\theta = r_\theta/S. \tag{3.4}$$

This standard approach involves the series expansion of the electric potential and an assumption of a relatively weak E_r. However, the applicability of this approach to plasma edge conditions has been questioned [73].

Although the term "orbit squeezing" is not usually associated with a constant radial electric field, even a constant E_r affects the orbit width. This happens because the $\boldsymbol{E}\times\boldsymbol{B}$ motion, particularly the toroidal drift with velocity E_r/B_θ, modifies the parallel velocity and the deviation from the mean flux surface. Also the bounce frequency and toroidal precession frequency are affected. Furthermore, since the trapping-untrapping boundary is modified, the introduction of an electric field can cause orbit transitions. [74]

The finding from ASCOT simulations reported in **Publication I** was that the orbit width of co- and counter-injected NBI ions is noticeably affected by a constant radial electric field. A constant E_r also affects the toroidal precession, and a strong enough E_r can even reverse it. A more extensive analysis using an experimentally obtained radial electric field is reported in **Publication VII**. The banana orbit width was found to be consistently reduced for counter-injected ions, and increased for co-injected ions. These results are illustrated in figure 3.2. Also the distribution of bounce time between the inner and outer legs was affected: the duration of the outer leg of orbit is consistently reduced compared to the duration of the inner leg. This effect, illustrated in figure 3.3, is the same for both injection directions. Orbit transitions from trapped to untrapped were observed for co-injection, whereas the converse transition was observed for counter-injection. Addditionally, the fraction of direct orbit losses was reduced when E_r was turned on.

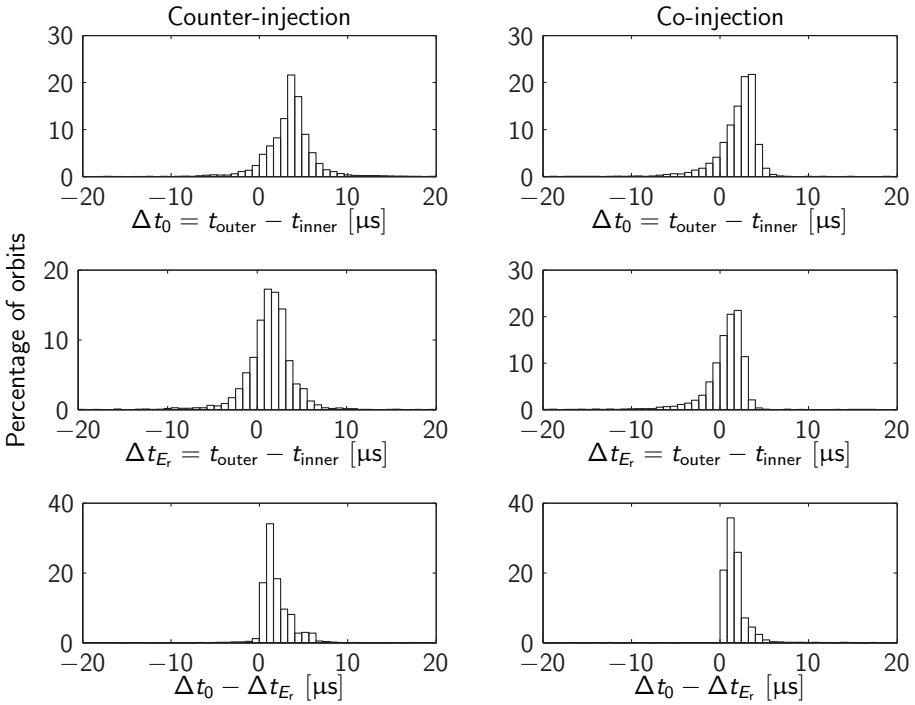

Figure 3.3: Top and middle row: histogram of the asymmetry of orbit leg duration, i.e., the difference of the duration of inner and outer banana orbit legs, for co- and counter-injected neutral beam ions, with and without radial electric field. Bottom row: histogram of the difference in the asymmetry with and without E_r. The duration of outer (inner) orbit leg is consistently decreased (increased) for both injection directions.

4 Application to AUG discharges

The ASCOT code was used to simulate counter-injected neutral beam ions in ASDEX Upgrade QH-mode discharge #17695 and co-injected neutral beam ions in a virtual discharge created from QH-mode discharge data by reversing the toroidal magnetic field, plasma current and test particle pitch. The objective was to compare the surface loads caused by beam ions and the edge fast ion distribution between co-injection and counter-injection in otherwise similar conditions. The effects of radial electric field and toroidal ripple were taken into account, both separately and combined. The initial test particle ensemble for the simulations was produced by the FAFNER code. For the detailed setup of the simulations, see **Publication III** and **Publication VII**.

As a separate issue, tritons created in deuterium-deuterium fusion reactions were simulated first for ASDEX Upgrade Improved H-mode discharge #17219 and later for the standard H-mode discharge #17216. The simulated tritium fluxes onto the surfaces were compared to the experimental surface distributions of tritium obtained by Photo-Stimulated Luminescence (PSL) measurements. The radial birth profiles of tritons from beam-target and thermal DD-fusion reactions were obtained from FAFNER-simulations provided by Max-Planck-Institut für Plasmaphysik, the institute conducting the AUG experiment, and the profiles were then used to create the test particle ensemble for ASCOT. The triton simulation setup is described in **Publication III**.

4.1 Surface loads

The surface loads caused by the co- and counter-injected neutral beam ions were addressed in **Publications II** and **III**. Due to a programming error affecting the collisions, the analysis had to be redone, but the correction did not have any striking effect on the results. The observed quantitative differences were reported in a corrigendum, **Publication V**. In the making of **Publication VII**, the simulations were redone once more, this time with a larger number of initial test particles from the FAFNER code. At the time it was discovered that earlier the FAFNER code had been run with parameters for an axisymmetric case, meaning that the test particles had been launched from an incorrect toroidal position with respect to the toroidal ripple. The correction did not affect the results significantly. This and the relatively small effect of the earlier correction indicate a certain robustness of the results.

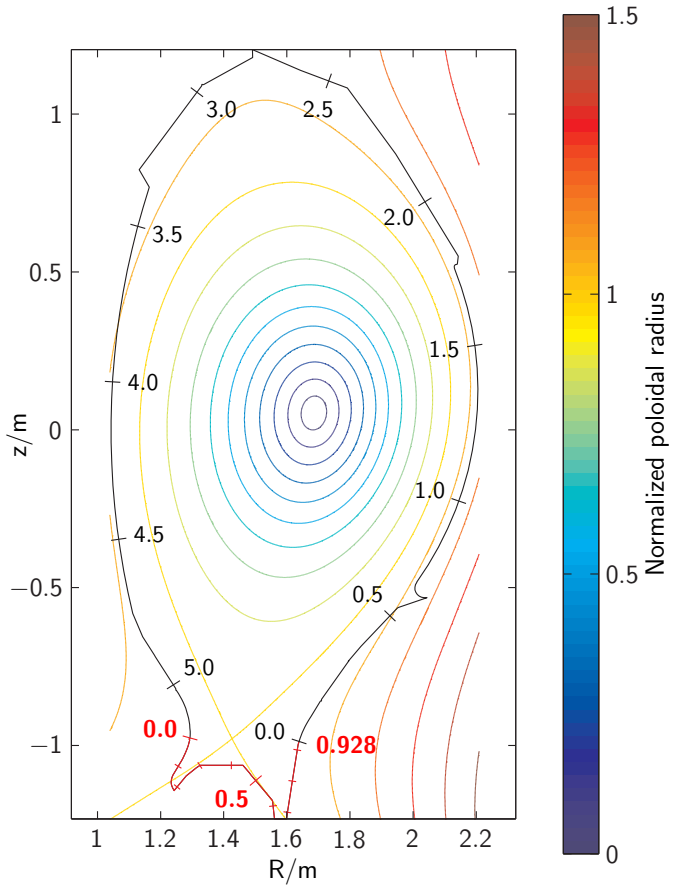

Figure 4.1: The AUG wall geometry used in the simulations and illustration of the wall and divertor coordinates. The flux surfaces of AUG discharge # 17695 at $t = 5.6\,\mathrm{s}$ are shown in color.

The wall load from counter-injected beams is substantial already in an axisymmetric magnetic field and it consists mainly of direct orbit losses, whereas for co-injection it is negligible in the absence of toroidal ripple. Ripple increases the wall load in both cases, but the load remains always much lower for co-injection. The effect of a radial electric field on the wall load is small, but the synergistic effect of ripple together with E_r increases it even more than ripple alone. The 2D wall loads for co- and counter-injection as a function of the toroidal angle and position along the wall (see figure 4.1), obtained in the analysis of **Publication VII**, are illustrated in figures 4.2 and 4.3, respectively. The numerical values in the figures are only indicative because the standard deviation exceeds 100 % almost everywhere. This does not, however, render the figures meaningless, because the regions with and without load can nevertheless be distinguished. The peak wall loads for co- and counter-injection are $(0.1 + 0.1 - 0.0)\,\mathrm{MW/m^2}$ and $(0.8 \pm 0.2)\,\mathrm{MW/m^2}$, respectively, obtained for the

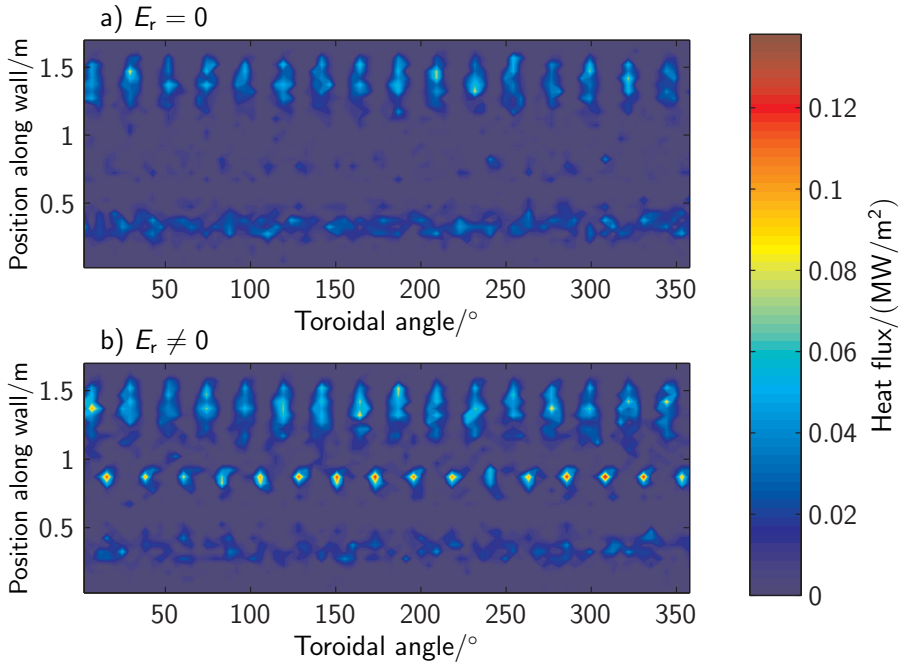

Figure 4.2: Comparison of the heat flux onto the walls for co-injection with toroidal ripple in the a) absence, and b) presence of a radial electric field. The periodic pattern due to ripple-trapping losses is clearly visible. The additional wall load caused by E_r shows as hot spots in the middle of the lower figure. In an axisymmetric magnetic field the wall load is practically non-existent.

case when both ripple and E_r are present. The upper and lower bounds are the maxima of the average heat flux $\bar{q}$ plus/minus one standard deviation:

$$\text{upper bound} = \max_{\text{surface}} (\bar{q} + \sigma) \tag{4.1}$$

$$\text{lower bound} = \max_{\text{surface}} (\bar{q} - \sigma)\,. \tag{4.2}$$

The divertor loads are illustrated in figures 4.4 and 4.5. For co-injection there is little variation in the divertor load when ripple and electric field are switched on and off, but for counter-injection the divertor load is clearly reduced in the presence of ripple, and even more when both ripple and E_r are nonzero. The radial electric field also decreases the peak divertor load for counter-injection: for $E_r = 0$, the peak load is $(0.6 + 0.5 - 0.2)\,\mathrm{MW/m^2}$, and with nonzero E_r it is $(0.3 + 0.4 - 0.1)\,\mathrm{MW/m^2}$ (case with ripple). The converse seems to be true for co-injection, but on closer inspection, the hot spots in figure 4.4 turn out to originate from first-orbit losses of very few test particles ionized mainly on the high-field side. Only few NBI particles, test or real, reach the high-field side to begin with. Therefore the hot spots are most likely

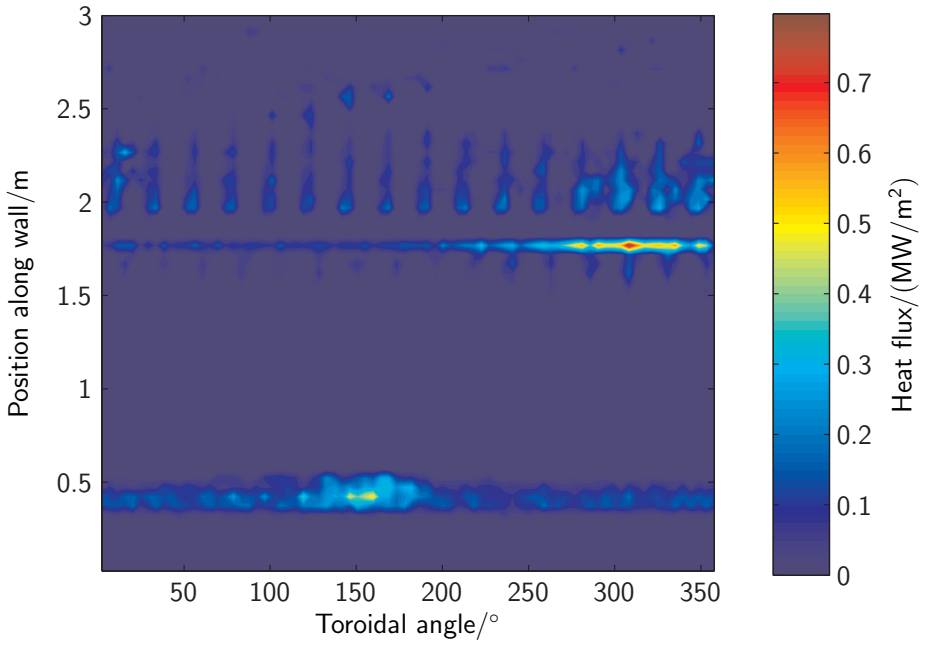

Figure 4.3: Heat flux onto the walls for counter-injection with both toroidal ripple and E_r present. The majority of the load consists of direct orbit losses which show the hot spots at $\phi \approx 150°$ and $\phi \approx 300°$. The ripple losses have a periodic pattern.

effected by the weak statistics on the high field side, and the real peak divertor load for co-injection is about $0.2\,\mathrm{MW/m^2}$.

4.2 Edge fast ion distribution

The fast ion distribution at ASDEX Upgrade edge was first addressed in publications **I** and **II**. Results of a more detailed analysis were reported in **Publication III**, but they turned out to be incorrect due to a programming error: only the carbon impurities were taken into account in the collision operator. The absence of electron and main-ion collisions lengthened the slowing-down time of NBI ions roughly by a factor of two which was directly reflected in the fast ion distribution. The corrected results were reported in **Publication VII**, now focusing especially on the effect of the radial electric field which became much more pronounced after the collision operator was fixed.

The fast ion density and its gradient are found to be higher for counter-injection than for co-injection in the edge region. For the former, particles ionized farther inside the plasma are fed into the edge region, while for the latter, the few particles

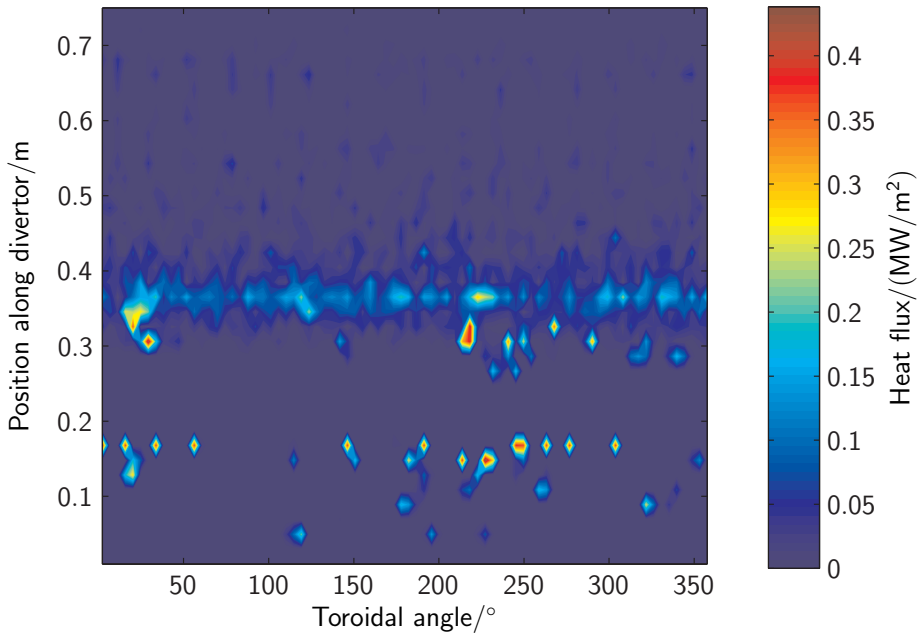

Figure 4.4: Divertor heat flux for co-injection with toroidal ripple and $E_r = 0$. The hot spots are due to direct losses of particles ionized on the high-field side.

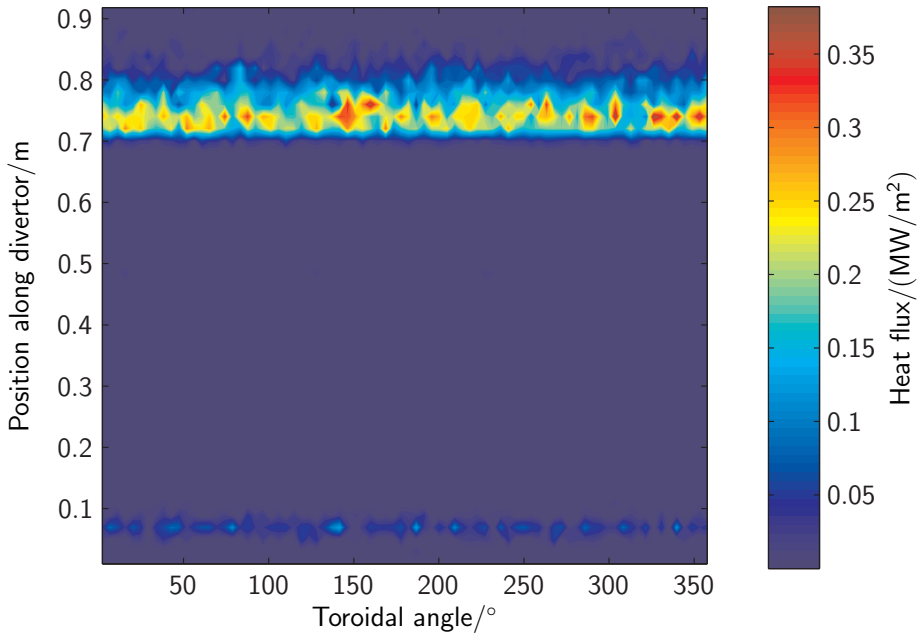

Figure 4.5: Divertor heat flux for counter-injection with nonzero ripple and E_r. The "belt" of weaker heat load in the lower part of the figure is not present when the radial electric field is off.

ionized in the edge region spend most of their time inward of their ionization point. For co-injection there exists also a population of passing particles near the edge. The same population does exist also for counter-injection, but farther inside the plasma due to the difference in the direction of $\nabla \boldsymbol{B}$-drift (see section 3.1).

The orbit transitions caused by the radial electric field (see section 3.3) result in increased edge density and density gradient for both injection directions. The effect of toroidal ripple is opposite. When both are present, their effects are canceled to some extent, especially for co-injection. The orbit transitions from trapped to passing occurring for co-injected particles strengthen the already existing population of passing particles in the edge region significantly. For counter-injection a smaller passing particle population is created by the same process from ions which have undergone sufficient pitch-angle scattering to change their direction.

4.3 DD-triton surface distribution

The first results of DD-triton simulations for ASDEX Upgrade were presented in **Publication II** and, together with comparison to experimental results, in **Publication III**. In **Publication IV**, the tritium inventory in a long-pulse or steady-state fusion reactor was discussed. The AUG triton analysis was continued in **Publication VI**.

Earlier findings on JT-60U [75] indicate that the tritium surface distribution reflects the energetic triton flux onto the surfaces. The results obtained for ASDEX Upgrade corroborate these findings: the simulated triton flux is in qualitative agreement with the measured tritium surface distribution. However, the comparison is problematic, because the measurement result corresponds to the time-integrated triton flux over one experimental campaign, including also the thermal contribution, while only one time instant of one discharge can be simulated at a time.

The first simulated discharge was an Improved H-mode one, because such discharges produce the most tritium, the majority of it coming from beam-target fusion reactions. In an attempt to take into account also the frequency of different types of discharges, a standard H-mode discharge was simulated. Unfortunately only later it was realized that the equilibria of the two discharges were quite similar, and in both the clearance between the separatrix and the wall was relatively large. This can in part explain why in the simulations the wall and divertor fluxes are similar in magnitude while the measured PSL intensity is an order of magnitude higher on the limiter than on the divertor. Another factor is the 2D wall used in the simulation which

artificially decreases the wall flux by dispersing it all around the torus. In reality the limiter and other similar protruding wall structures are toroidally localized.

Although DD-fusion tritium is not particularly significant in present experiments, it deserves careful consideration in future fusion reactors due to its high birth energy and deep penetration in materials. The thermal fuel tritium will of course be present in more copious amounts, but nevertheless also DD-tritons can contribute both to material damage and total tritium inventory. From the modelling point of view, the triton simulations and comparison to measured tritium distribution could serve as benchmark for fusion alpha simulations because the behaviour of DD-tritons and fusion alphas is similar. However, an attempt to obtain results of the dependency between triton flux and tritium surface distribution and to benchmark the code at the same time would border on circular logic.

5 Discussion and outlook

The main results obtained in this thesis are related to the QH-mode of ASDEX Upgrade. The surface loads and edge fast ion distribution from co- and counter-injected neutral beams have been analyzed by means of orbit-following simulations, taking into account the effects of toroidal ripple and radial electric field. Confinement of fast particles will be of great importance for burning plasma experiment in the future, and many fast ion studies have been performed, e.g., [76–78], or are being performed, e.g., [60].

The importance of analysis performed here is its connection to the QH-mode. To date, QH-mode has been achieved only by using counter-injected neutral beams which are known to be prone to higher losses than co-injected beams due to the unfavorable direction of the gradient drift. Therefore, one consequence of pursuing the QH-mode is higher surface load at the wall structures, a result confirmed in this thesis. The effort is, nevertheless, well spent because the transient loads caused by ELMs are a serious handicap of the standard H-mode. Tailoring a different kind of stationary, ELM-free H-mode without the use of counter-injected beams may become possible once the ELM suppression mechanism in the QH-mode is understood.

The edge fast ion distribution, the second subject of the QH-mode studies in the thesis, may well be related to the roots of the QH-mode. Different injection directions of the neutral beams lead to different fast ion distribution at the edge. The implications of this on the stability properties of the edge could be evaluated by using the 4D distribution functions obtained in the present analysis as input for MHD stability codes. Another, simpler mechanism affecting the edge in QH-mode could be a resonance between fast ions and the edge harmonic oscillations. This could be possible for a fraction of the fast ions for which the toroidal precession has been reversed by the radial electric field. The 4D distribution function and the data already obtained about the collisionless orbits of the neutral beam ions could be used to analyze this in more detail.

In the course of the QH-mode modelling, it has become apparent that the effect of radial electric field is very often presumed to be only the orbit-squeezing due to its gradient. The fact that also a constant electric field modifies the orbit width seems to be somewhat neglected. Furthermore, the analysis of collisionless orbits performed here shows that for neutral beam ions, the effect of E_r on orbit width depends on the injection direction, and, in particular, the orbits of co-injected ions are consistently widened. Either the squeezing parameter becomes smaller than

one, indicating widening instead of squeezing, or the series expansion approach used to derive the orbit-squeezing parameter is not applicable, as suggested by Krasheninnikov *et al.* [73]. However, the effects of E_r on fast ion distribution are more conclusively explained by the E_r-induced orbit transitions than orbit-width effects.

The modelling of DD-fusion tritons has not been completed yet, but a qualitative agreement between the simulated triton flux and measured tritium surface distribution has been obtained already. This in in line with the earlier findings obtained at JT-60U tokamak [75]. The analysis will be continued by simulating a larger set of different discharges more representative of the whole operational campaign.

ASCOT code, the modelling tool used in the above analysis, is best suited for neoclassical studies, although a simple model for anomalous transport has been implemented. Consequently, the possible effect of turbulence on fast ions has been neglected. There are indications that small scale turbulence may have an effect on fast ions [43], but so far no compelling experimental evidence or reliable theoritical models exist. If such evidence should be found and better models be developed in the future, the present analysis can be repeated taking into account also the anomalous transport of fast ions.

References

[1] JET Team (1992). Fusion energy production from a deuterium-tritium plasma in the JET tokamak. *Nuclear Fusion* **32**(2) 187–203.

[2] J. D. Strachan *et al.* (1994). Fusion power production from TFTR plasmas fueled with deuterium and tritium. *Physical Review Letters* **72**(22) 3526–3529.

[3] JET Team (1999). Physics of high performance JET plasmas in DT. *Nuclear Fusion* **39**(9Y) 1227–1244.

[4] R. Aymar, V. A. Chuyanov, M. Huguet, Y. Shinomura, ITER Joint Central Team, and ITER Home Teams (2001). Overview of ITER-FEAT — The future international burning plasma experiment. *Nuclear Fusion* **41**(10) 1301–1310.

[5] M. Keilhacker *et al.* (1984). Confinement studies in L and H-type ASDEX discharges. *Plasma Physics and Controlled Fusion* **26**(1A) 49–63.

[6] H. Zohm (1996). Edge localized modes (ELMs). *Plasma Physics and Controlled Fusion* **38**(2) 105–128.

[7] J. W. Connor (1998). A review of models for ELMs. *Plasma Physics and Controlled Fusion* **40**(2) 191–213.

[8] F. Wagner *et al.* (1982). Regime of improved confinement and high beta in neutral-beam-heated divertor discharges of the ASDEX tokamak. *Physical Review Letters* **49**(19) 1408–1412.

[9] W. W. Heidbrink and G. J. Sadler (1994). The behaviour of fast ions in tokamak experiments. *Nuclear Fusion* **34**(4) 535–615.

[10] K. McGuire *et al.* (1983). Study of high-beta magnetohydrodynamic modes and fast-ion losses in PDX. *Physical Review Letters* **50**(12) 891–895.

[11] L. Chen, R. B. White, and M. N. Rosenbluth (1984). Excitation of internal kink modes by trapped energetic beam ions. *Physical Review Letters* **52**(13) 1122–1125.

[12] G. Y. Fu and J. W. Van Dam (1989). Excitation of the toroidicity-induced shear Alfvén eigenmode by fusion alpha particles in an ignited tokamak. *Physics of Fluids B: Plasma Physics* **1**(10) 1949–1952.

[13] K. L. Wong *et al.* (1991). Excitation of toroidal Alfvén eigenmodes in TFTR. *Physical Review Letters* **66**(14) 1874–1877.

[14] S. Ali-Arshad and D. J. Campbell (1995). Observation of TAE activity in JET. *Plasma Physics and Controlled Fusion* **37**(7) 715–722.

[15] F. Porcelli (1991). Fast particle stabilisation. *Plasma Physics and Controlled Fusion* **32**(13) 1601–1620.

[16] M. García-Muñoz, P. Martin, H.-U. Fahrbach, M. Gobbin, S. Günter, M. Maraschek, L. Marrelli, H. Zohm, and the ASDEX Upgrade Team (2007). NTM induced fast ion losses in ASDEX Upgrade. *Nuclear Fusion* **47**(7) L10–L15.

[17] K. H. Burrell *et al.* (2002). Quiescent H-mode plasmas in the DIII-D tokamak. *Plasma Physics and Controlled Fusion* **44**(5A) A253–A263.

[18] J. L. Luxon and L. G. Davis (1985). Big Dee – a flexible facility operating near breakeven conditions. *Fusion Technology* **8**(1) 441–449.

[19] W. Suttrop *et al.* (2003). ELM-free stationary H-mode plasmas in the ASDEX Upgrade tokamak. *Plasma Physics and Controlled Fusion* **45**(8) 1399–1416.

[20] M. Kaufmann *et al.* (1993). Edge physics and H-mode studies in ASDEX Upgrade. *Plasma Physics and Controlled Fusion* **36**(SB) B205–B214.

[21] J. A. Heikkinen, S. K. Sipilä, and T. J. H. Pättikangas (1993). Monte Carlo simulation of runaway electrons in a toroidal geometry. *Computer Physics Communications* **76**(2) 215–230.

[22] J. A. Heikkinen and S. K. Sipilä (1995). Power transfer and current generation of fast ions with large-k_θ waves in tokamak plasmas. *Physics of Plasmas* **2**(10) 3724–3733.

[23] S. Sipilä (1997). *Monte Carlo simulation of charged particle orbits in the presence of radiofrequency waves in tokamak plasmas*. Ph.D. thesis, Department of Engineering Physics and Mathematics, Helsinki University of Technology, Espoo, Finland.

[24] K. Tani, M. Azumi, H. Kishimoto, and S. Tamura (1981). Effect of toroidal field ripple on fast ion behaviour in a tokamak. *Journal of the Physical Society of Japan* **50**(5) 1726–1737.

[25] R. B. White and M. S. Chance (1984). Hamiltonian guiding center drift orbit calculations for plasma of arbitrary cross sections. *Physics of Fluids* **27**(10) 2455–2467.

[26] R. B. White and A. H. Boozer (1995). Rapid guiding center calculations. *Physics of Plasmas* **2**(8) 2915–2919.

[27] G. G. Lister (1985). FAFNER: A fully 3-D neutral beam injection code using Monte Carlo methods. Technical Report IPP 4/222, Max-Planck-Institut für Plasmaphysik, Garching, Germany.

[28] A. Teubel and F. P. Penningsfeld (1994). Influence of radial electric fields on the heating efficiency of neutral beam injection in the W7-AS stellarator. *Plasma Physics and Controlled Fusion* **36**(1) 143–152.

[29] A. Teubel (1994). FAFNER2: 3-D 'flux coordinate' neutral beam injection code using Monte Carlo methods. Technical Report IPP 4/266, Max-Planck-Institut für Plasmaphysik, Garching, Germany.

[30] A. Pankin, D. McCune, R. Andre, G. Bateman, and A. Kritz (2004). The tokamak Monte Carlo fast ion module NUBEAM in the National Transport Code Collaboration library. *Computer Physics Communications* **159**(3) 157–184.

[31] E. Strumberger (2000). Deposition patterns of fast ions on plasma facing components in W7-X. *Nuclear Fusion* **40**(10) 1697–1713.

[32] M. Schneider, L.-G. Eriksson, V. Basiuk, and F. Imbeaux (2005). On alpha particle effects in tokamaks with a current hole. *Plasma Physics and Controlled Fusion* **47**(12) 2087–2106.

[33] J. Wesson (2004). *Tokamaks*. Oxford University Press, New York, third edn.

[34] A. H. Boozer (1980). Guiding center drift equations. *Physics of Fluids* **23**(5) 904–908.

[35] A. H. Boozer (1983). Transport and isomorphic equilibria. *Physics of Fluids* **26**(2) 496–499.

[36] J. R. Cash and A. H. Karp (1990). A variable order Runge-Kutta method for initial value problems with rapidly varying right-hand sides. *ACM Transactions on Mathematical Software* **16**(3) 201–222.

[37] A. H. Boozer and G. Kuo-Petravic (1981). Monte Carlo evaluation of transport coefficients. *Physics of Fluids* **24**(5) 851–859.

[38] M. N. Rosenbluth, R. D. Hazeltine, and F. L. Hinton (1972). Plasma transport in toroidal confinement systems. *Physics of Fluids* **15**(1) 116–140.

[39] R. Balescu (1960). Irreversible processes in ionized gases. *Physics of Fluids* **3**(1) 52–63.

[40] A. Lenard (1960). On Bogoliubov's kinetic equation for a spatially homogeneous plasma. *Annals of Physics (NY)* **10**(3) 390–400.

[41] J. A. Heikkinen, S. J. Karttunen, T. J. H. Pättikangas, and S. K. Sipilä (1993). Runaway losses in current ramp-up with lower hybrid waves. *Nuclear Fusion* **33**(6) 887–894.

[42] S. K. Sipilä and J. A. Heikkinen (1994). Monte Carlo simulation of lower hybrid current drive in tokamaks. *IEEE Transactions on Plasma Science* **22**(3) 260–266.

[43] S. Günter *et al.* (2007). Interaction of energetic particles with large and small scale instabilities. *Nuclear Fusion* **47**(8) 920–928.

[44] T. H. Stix (1975). Fast-wave heating of a two-component plasma. *Nuclear Fusion* **15**(5) 737–754.

[45] J. A. Heikkinen and S. K. Sipilä (1995). α-particle transport-driven current in tokamaks. *Physical Review E* **51**(3) R1655–R1658.

[46] J. A. Heikkinen and S. K. Sipilä (1997). Monte Carlo simulation of minority ion bootstrap current by off-axis ion cyclotron heating in tokamaks. *Nuclear Fusion* **37**(6) 835–849.

[47] T. Kurki-Suonio, S. I. Lashkul, and J. A. Heikkinen (2002). Formation and detection of internal transport barriers in low-current tokamaks. *Plasma Physics and Controlled Fusion* **44**(3) 301–323.

[48] R. J. Goldston, D. C. McCune, H. H. Towner, S. L. Davis, R. J. Hawryluk, and G. L. Schmidt (1981). New techniques for calculating heat and particle source rates due to neutral beam injection in axisymmetric tokamaks. *Journal of Computational Physics* **43**(1) 61–78.

[49] G. Marsaglia, A. Zaman, and W. W. Tsang (1990). Toward a universal random number generator. *Statistics and Probability Letters* **9**(1) 35–39.

[50] S. Ma, R. D. Sydora, and J. M. Dawson (1993). Binary collision model in gyrokinetic simulation plasmas. *Computer Physics Communications* **77**(2) 190–206.

[51] T. P. Kiviniemi, J. A. Heikkinen, and A. G. Peeters (2000). Test particle simulation of nonambipolar ion diffusion in tokamaks. *Nuclear Fusion* **40**(9) 1587–1596.

[52] J. A. Heikkinen, T. P. Kiviniemi, and A. G. Peeters (2000). Neoclassical radial current balance in tokamaks and transition to the *H* mode. *Physical Review Letters* **84**(3) 487–490.

[53] J. A. Heikkinen, T. P. Kiviniemi, T. Kurki-Suonio, A. G. Peeters, and S. K. Sipilä (2001). Particle simulation of the neoclassical plasmas. *Journal of Computational Physics* **173**(2) 527–548.

[54] J. Cornelis, R. Sporken, G. van Oost, and R. R. Weynants (1994). Predicting the radial electric field imposed by externally driven radial currents in tokamaks. *Nuclear Fusion* **34**(2) 171–183.

[55] T. Kurki-Suonio, T. P. Kiviniemi, S. K. Sipilä, J. A. Heikkinen, W. Fundamenski, G. F. Matthews, and V. Riccardo (2002). Monte Carlo simulations of the heat load asymmetries on JET divertor plates. *Nuclear Fusion* **42**(6) 725–732.

[56] R. Schneider, X. Bonnin, K. Borrass, D. P. Coster, H. Kastelewicz, D. Reiter, V. A. Rozhansky, and B. J. Braams (2006). Plasma edge physics with B2-Eirene. *Contributions to Plasma Physics* **46**(1–2) 3–191.

[57] D. McDonald and E. Springmann (2003). *FLUSH — User guide*. `http://users.jet.efda.org/pages/codes-data/flush/FLUSH_manual.pdf`, accessed 2008-01-22.

[58] KK–subroutines (SunOS, Solaris, Aix, UniCos). `https://www.aug.ipp.mpg.de/aug/manuals/Asubrout.txt`, version 4.1, 2007.03. Accessed 2008-01-22 (Account at IPP required).

[59] P. C. de Vries *et al.* (2008). Effect of toroidal field ripple on plasma rotation in JET. *Nuclear Fusion* **48**(3) 035 007 (6 pp).

[60] EFDA task TW6-TPO-RIPLOS: 3-D calculations of ion losses and wall loads in ITER due to toroidal field ripple.

[61] D. Badouel (1993). An efficient ray-polygon intersection. In A. S. Glassner (ed.), *Graphics Gems*, pp. 390–393, Academic Press, Boston (MA).

[62] C. Challis, J. Cordey, H. Hamnen, P. Stubberfield, J. Christiansen, E. Lazzaro, D. Muir, D. Stork, and E. Thompson (1989). Non-inductively driven currents in JET. *Nuclear Fusion* **29**(4) 563–570.

[63] J. A. Heikkinen, W. Herrmann, and T. Kurki-Suonio (1997). The effect of a radial electric field on ripple-trapped ions observed by neutral particle fluxes. *Physics of Plasmas* **4**(10) 3655–3662.

[64] T. Kurki-Suonio, V. Hynönen, W. Suttrop, H.-U. Fahrbach, J. Stober, and the ASDEX Upgrade Team (2006). Edge fast ion distribution – benchmarking ASCOT against experimental NPA data on ASDEX Upgrade. In F. De Marco and G. Vlad (eds.), *Proceedings of the 33rd European Physical Society Conference on Plasma Physics, Rome, Italy, June 19–23, 2006, Europhysics Conference Abstracts*, vol. 30I, pp. P–2.145 (4 pp), European Physical Society, Rome, Italy.

[65] G. Bracco and K. Günther (1985). H/D measurement by neutral particle analysis at JET. Technical Report JET-R(96)04, JET Joint Undertaking, Abingdon, Oxfordshire, OX14 3EA, UK.

[66] L.-G. Eriksson and F. Porcelli (2001). Dynamics of energetic ion orbits in magnetically confined plasmas. *Plasma Physics and Controlled Fusion* **43**(4) R145–R182.

[67] T. E. Stringer (1972). Effect of the magnetic field ripple on diffusion in tokamaks. *Nuclear Fusion* **12**(6) 689–694.

[68] O. A. Andersson and H. P. Furth (1972). Imperfect axisymmetry in the tokamak configuration. *Nuclear Fusion* **12**(2) 207–213.

[69] R. B. White, R. J. Goldston, M. H. Redi, and R. V. Budny (1996). Ripple-induced energetic particle loss in tokamaks. *Physics of Plasmas* **3**(8) 3043–3054.

[70] R. B. White (1998). Chaos in trapped particle orbits. *Physical Review E* **58**(2) 1774–1779.

[71] B. V. Chirikov (1979). A universal instability of many-dimensional oscillator systems. *Physics Reports* **52**(5) 263–379.

[72] R. D. Hazeltine (1989). Self-consistent radial sheath. *Physics of Fluids B: Plasma Physics* **1**(10) 2031–2039.

[73] S. I. Krasheninnikov and P. N. Yushmanov (1994). The influence of a radial electric field on neoclassical orbits and ion prompt losses from tokamak edge plasmas. *Physics of Plasmas* **1**(5) 1186–1194.

[74] K. Itoh and S.-I. Itoh (1996). The role of electric field in confinement. *Plasma Physics and Controlled Fusion* **38**(1) 1–49.

[75] K. Masaki *et al.* (2003). Tritium distribution in JT-60U W-shaped divertor. *Journal of Nuclear Materials* **313–316** 514–518.

[76] K. Tobita *et al.* (1995). Ripple induced fast ion loss and related effects in JT-60U. *Nuclear Fusion* **35**(12) 1585–1591.

[77] S. D. Pinches *et al.* (2006). Observation and modelling of fast ion loss in JET and ASDEX Upgrade. *Nuclear Fusion* **46**(10) S904–S910.

[78] E. Strumberger, S. Günter, E. Schwarz, C. Tichmann, and the ASDEX Upgrade Team (2008). Fast particle losses due to NTMs and magnetic field ripple. *New Journal of Physics* **10** 023 017 (21 pp).

Appendix A Generation of distributions

In ASCOT simulations, an ensemble of test particles represents a population of physical particles. Each test particle is simulated until one of the following end criteria is reached:

1) the specified particle tracing time $T_{\max}$ is exceeded

2) maximum CPU time per test particle is exceeded

3) the specified lower limit for energy is reached

4) particle hits the wall or divertor

5) particle escapes from plasma

6) the specified number of orbits have been calculated

In most simulations the conditions 5 and 6 are disabled. If the self-consistent radial electric field or the binary collision model is enabled, $T_{\max}$ is replaced by the global time step and test particles that are lost to the wall or divertor are regenerated at the separatrix. Once all test particles have completed one global time step, the radial electric field is updated or the binary collisions are evaluated. The simulation continues in this manner until $T_{\max}$ is exceeded. Information about each integration time step is accumulated into various distributions, and in the end the summed contribution of all test particles is normalized to physical units by appropriately scaling the distributions.

For practical reasons, the accumulation of distributions is limited to a rectangular region in phase space. The coordinates typically used are (ρ, θ) or (R, z) in the configuration space, and $(v_\parallel, v_\perp)$ or (ϵ, ξ) in the velocity space. The radial coordinate ρ is special in that it has several limits:

- minimum and maximum initial ρ of test particles
- lower and upper ρ-limits of self-consistent radial electric field model, ρ_{1,E_r} and ρ_{2,E_r},
- lower and upper ρ-limits for distributions, ρ_1 and ρ_2.

Information is gathered into the distributions only inside ρ_1 and ρ_2, but the particle orbits are simulated also outside this interval. If the self-consistent radial electric field model is used, only the time spent inside ρ_{1,E_r} and ρ_{2,E_r} can invoke quitting condition 1. To avoid boundary effects, it is advisable that ρ_1 and ρ_2 are inside the other two ρ-limits. The simulation time can be divided into at most twenty time slices which allow the study of time-dependent phenomena. However, steady-state simulations are much more common than truely time-dependent ones, so in most cases the time-slicing is used only for diagnostic purposes.

The number of physical particles one test particle represents is controlled by the ratio of the physical particle abundance to the test particle ensemble size, $R_\mathrm{real/test}$, and the weight of the test particle. With these definitions, the product of $R_\mathrm{real/test}$ and the number of test particles, N_part, is either the number of real particles or the source rate, depending on the type of simulation. In the latter case, the unit of $R_\mathrm{real/test}$ is s^{-1}. This does not affect the simulation itself in any way, but normalizations needed for the distributions are different. Another factor in the normalization is the particle regeneration. As an example, let us consider the average particle density in a phase space cell, i.e. the number of particles inside the cell divided by the volume of the cell. The quantity accumulated during the simulation in this case is T_cell, the time a test particles spends inside a phase space cell multiplied by the weight of the particle and the acceleration factor used. This has to be converted to the number of physical particles. There are three meaningful combinations of regeneration and the type of the simulation:

1. *Fixed number of particle that are regenerated, e.g. a thermal bulk plasma simulation with self-consistent radial electric field.* The accumulated time T_cell divided by T_tot, the sum of individual T_cell over all cells, represents the fraction of particles residing in a particular phase space cell. This multiplied by the number of real particles, $N_\mathrm{part} \times R_\mathrm{real/test}$, yields the number of physical particles in the cell.

   This kind of simulation is steady-state by definition, but usually there is a transient phase in the beginning before the steady-state is reached. For this reason, the time-slicing is used and the slices from the transient part of the simulation are neglected.

2. *Fixed number of particles that are not regenerated, e.g. a pellet.* This is the only truely time-dependent situation, and time-slicing is not only possible but necessary. Since the number of particles is allowed to decrease, $T_\mathrm{cell}/T_\mathrm{tot}$ is no

longer meaningful, and division by the length of the time slice, T_{slice}, is used instead. Multiplication only by $R_{\mathrm{real/test}}$ is required to obtain the number of particles inside the cell because the dependence on N_{part} is already included in $T_{\mathrm{cell}}/T_{\mathrm{tot}}$.

3. *Particle source simulation, e.g. neutral beam injection or alpha particles.* A particle source simulation is steady-state by definition, and regeneration of particles must not be used. Time-slicing is not physically meaningful but it can be used for code-diagnostic purposes. The simulation time T_{max} has to be long enough for all test particles to slow down close to thermal energy. The lower limit of energy in quitting condition 3 is usually set to twice the local thermal energy. The number of particles inside a cell is simply T_{cell} multiplied by $R_{\mathrm{real/test}}$.

The final step in all above cases is division by the phase space cell volume. There have been no practical applications for the fourth technically possible combination, regeneration with a particle source. Although the accumulated quantity varies depending on the distribution, the same normalizations apply in almost all circumstances. The toroidal and poloidal velocity and the parallel current distributions are exceptions since they are essentially time-weighted averages of toroidal, poloidal, and parallel velocities, respectively. The radial charge fluence, being a time-integral of radial current, is not applicable to source simulations.

Appendix B Examples of ASCOT IO-files

B.1 Particle initial data file

```
PARTICLE INITIAL DATA FOR ASCOT
==============================

IPSPEC - Plasma species identifier
ENERG1 - Energy of particle (eV)
PITCH1 - Pitch angle cosine of particle
RHO1   - Magnetic surface of particle (0...1)
THETA1 - Boozer poloidal angle of particle (deg)
PHI1   - Toroidal angle of particle (deg)
R1     - R of particle (m)
Z1     - z of particle (m)
WEIGHT - Weight factor of particle
PARTNO - Number of particle

Number of particles in ensemble:    9965       Simulation type: 5
Actual number(s) or source rate(s) of species:
 0.00000D+00  0.75000D+21  0.00000D+00

Number of rho surfaces:  999     rho1, rho2:   0.00000       1.00000
Number of theta angles:  999
Number of phi angles:    999
Number of pitches:       999

2   60000.      0.41280      0.45328       359.36       333.61
 1.8627      0.49809E-01   1.0000             1
2   60000.      0.31231      0.75599       343.53       333.62
 1.9402     -0.14283       1.0003             2
[list continues]
```

B.2 Console file

```
Machine epsilon =   2.2204460492503131E-016

CPU time limit for process (s):    1700.000
```

```
NOTE: No MHD mode data found.

Reading wall/divertor location data...

AUG discharge #        17695  at t =    5.600000     s

Reading scalar values...
Reading radial profiles...
Reading magnetic background array (          600 ,          600 )...
Searching for magnetic axis...

Plasma current (A):                                  -998684.
Toroidal magnetic field at geometric centre (T):      1.99782
Geometric centre (R,z):                               1.62640     -0.859125E-01
Minor radius along equator:                          0.492522
Elongation:                                           1.76643
Limiter psi and rho (not in use):                    0.305208       1.14315

Axis location (R,z):       1.68615      0.533165E-01
X-point location (R,z):    1.42635     -0.978621

Determining outermost closed flux surface psi:
closed flux surface at PSISEP =   0.2335536     ...failed...
closed flux surface at PSISEP =   0.2335303     ...OK!

Psi and rho for coordinate system switch:  0.231212      0.995000
Outermost psi and rho of (psi,theta) grid:  0.233530      0.999973

Particle densities at centre of plasma (1/m^3):
-----------------------------------------------
electron    0.491367E+20
deuterium   0.393093E+20
carbon      0.163789E+19

Reading R derivatives of magnetic field...
Reading z derivatives of magnetic field...

Reading psi-dependent profiles...
Reading (psi,theta) background grid...
```

```
Found wall point with RHO < RHOLIM. Setting new value RHOLIM =    1.015287


NOTE: no SOL data found.

Number of particles in ensemble:         9965

Input complete.
```

B.3 Console_p file

```
Particle, end code, CPU, tot. CPU (s):     32  3   1.828       1.828

Particle, end code, CPU, tot. CPU (s):     64  3  0.3556       2.184

Particle, end code, CPU, tot. CPU (s):     96  3  0.6322       2.818

Particle, end code, CPU, tot. CPU (s):    128  3  0.6994       3.518

[list continues]
```

B.4 Logfile_p file

```
Particle     32/   9965 --  local thermal energy *    2.000000
Trapped/untrapped orbits:               43/      2246    Weight:  0.9999
Average bounce time (s):         0.1554E-04
Time/CPU/total CPU (s):     0.3805E-01(  0.3805E-01)/   1.828    /   1.828

Particle     64/   9965 --  local thermal energy *    2.000000
Trapped/untrapped orbits:              544/         8    Weight:   1.005
Average bounce time (s):         0.5872E-04
Time/CPU/total CPU (s):     0.2387E-01(  0.2387E-01)/  0.3556    /   2.184

Particle     96/   9965 --  local thermal energy *    2.000000
Trapped/untrapped orbits:               20/      1122    Weight:  0.9904
Average bounce time (s):         0.1788E-04
Time/CPU/total CPU (s):     0.1667E-01(  0.1667E-01)/  0.6322    /   2.818

[list continues]
```

B.5 Summary file

```
Summary:

Thermal particles                        7751
Divertor particles                       1223
   area            1 :         1223
Vessel wall particles                     991

Number of particles                      9965

Orbit loss particles                     2214
Percentage of 'orbit' losses in
Pfirsch-Schlueter region:          0.000

Total number of steps:                                 483357879
Total number of orbits:                 18538869
Average time step shrink factor:   1.000
Average particle confinement time (s):  0.1135E-01
Total CPU time (s):                        0.1386E+05
Average simulated time per particle (s):  0.3451E-01
```

ISBN 978-951-22-9458-9
ISBN 978-951-22-9459-6 (PDF)
ISSN 1795-2239
ISSN 1795-4584 (PDF)